WILEY | Hindawi

Research Article

Bridge Frequency Scanning Using the Contact-Point Response of an Instrumented 3D Vehicle: Theory and Numerical Simulation

Zhenkun Li [ID]**, Weiwei Lin** [ID]**, and Youqi Zhang** [ID]

Department of Civil Engineering, Aalto University, Rakentajanaukio 4 A, Espoo 02150, Finland

Correspondence should be addressed to Weiwei Lin; weiwei.lin@aalto.fi

Scanning the bridge's frequencies from the passing vehicle's vibration data has been frequently investigated recently. However, in previous studies, vehicles were typically simplified to quarter- or half-car models, and apparent disparity could be observed between the models and real vehicles. To make the vehicle model more practical, in this study, a 3D vehicle model is built to extract the bridge's frequencies from vehicle vibrations. For the first time, equations for calculating the contact-point (CP) response of the 3D vehicle model are derived with tire damping. Furthermore, residual CP responses between front and rear wheels are utilized to eliminate the inverse effects of road roughness, making the bridge frequencies outstanding in the frequency domain. The robustness of the proposed method is tested under different influence factors, and two possible measurement errors are as follows: the sensor position and axle distance when applying the proposed method in engineering. Results show that the proposed method performs stably under the influence of different road roughness classes and tire damping. Bridge frequencies can be identified when the vehicle is travelling at a highway speed (108 km/h in this study). Environmental noises can submerge the bridge's high-order frequencies but have little influence on the low-frequency range. High bridge damping will restrain the transmission of bridge vibration to the vehicle, making high-order bridge frequencies less visible. In addition, the errors introduced by a vehicle body sensor position can be eliminated when calculating the CP responses for tires, thus will not influence bridge frequency identification. To avoid possible errors induced by manual measurement of the axle distance, a novel cross-correlation function-based method is employed, which is verified effective and practical for calculating residual CP responses.

1. Introduction

Bridges are essential infrastructures connecting the traffic system all over the world. For monitoring purposes, the modal parameters of the bridge are universally investigated to evaluate its health conditions [1–3]. Natural frequency, as the fundamental dynamic property, can provide key health information of bridges. Mature approaches have been developed to obtain the bridge's frequencies using sensors deployed on the bridge structure (namely, the direct method). However, several problems are encountered when applying the direct method in practical engineering. First, to monitor the bridge at discrete points, a large number of sensors need to be installed to form a sensing network, which is undoubtedly expensive and time-consuming. Due to this reason, long-span or greatly important bridges are preferentially considered to install such a system rather than bridges in short or middle span, which, however, are the majority of the bridge system. Also, the sensor network generally needs to be installed in the construction stage. If an existing bridge needs to be equipped with sensors, a traffic pause may be required for days or weeks, which is not practical for bridges with heavy traffic [4]. As the number of newly constructed bridges is increasing and the old ones built in the last century are deteriorating, there is a great demand for methods to rapidly determine bridges' frequencies.

To solve the problems mentioned above, scanning the bridge's modal parameters indirectly (namely, vehicle scanning method, VSM) using the passing vehicle's vibration data was initially proposed by Yang et al. in 2004 [5]. In this study, the bridge's fundamental frequency was

successfully identified from a mass-spring model with one degree of freedom (DOF). The VSM method only needs a few sensors installed on the passing vehicle, thus is more economical compared to the direct method. In addition, the proposed method can fit various bridges and thus can be potential to extract a large number of bridges' frequencies rapidly without interrupting the ongoing traffic. Due to the above reasons, the characteristics of the VSM idea attract much interest from scholars all over the world [6, 7].

In the last two decades, it had been proved that the bridge's frequencies, modal shapes, and damping ratios could be scanned from the passing vehicle's vibration data [8], among which the extraction of bridge frequencies from the vehicle's accelerations was investigated most frequently. After the pioneer research [5], the existence of the bridge's dynamic information in the vehicle's vibrations was later confirmed by many simulations and experiments [9–13]. Since the vibrations are recorded by vehicles, their own frequencies will pollute the bridge frequency identification results. Naturally, it could be understood that if the vehicle's frequencies could be filtered out, the bridge's frequencies would be outstanding [14]. However, applying this idea normally requires the predetermined vehicle's frequencies. Later, data preprocessing methods in the time domain were employed, such as empirical mode decomposition (EMD) [15], ensemble empirical mode decomposition (EEMD) [16], and variational mode decomposition (VMD) [17]. Data processing in the time domain is intuitionistic and can be a powerful tool. However, the vehicle's dynamic properties need to be studied well in advance so that the researcher can identify the bridge's frequencies manually after the signal decomposition. The analysis methods went towards operational modal analysis (OMA) techniques soon. Stochastic subspace identification (SSI), one of the powerful frequency identification tools for frequency identification, was first adopted [18]. Other tools such as peak picking (PP) and frequency domain decomposition (FDD) were also proved effective for identifying the frequencies of the vehicle and bridge [19]. Notwithstanding, it was always difficult to identify the bridge's frequencies using one vehicle passage in the frequency domain due to the influence of vehicle frequencies and road roughness.

In the above studies, the identification of the bridge's frequencies is always impacted by the vehicle's frequencies. Besides, the extraction of the bridge's frequencies could be inversely influenced by the road's roughness. To solve the above two key problems, at first, the vehicle's parameters were studied. It was found that high vehicle damping [20], the increase of vehicle body mass [21], and heavy vehicles [22] could help suppress the vehicle frequency and the effect of road roughness, making the bridge's fundamental frequency highlighted. To eliminate the effects of the vehicle's self-vibration parameters, Shirzad-Ghaleroudkhani and Gül [23] tried to drive the vehicle off the bridge at first and then on the bridge to inversely filter out the vehicle's frequencies. To overcome the inverse effects of high vehicle speed, wavelet transform, and Hilbert transform were utilized to increase the frequency resolution of vehicle accelerations

[24, 25]. Shi and Uddin [26] systematically researched the effects of different parameters in the vehicle bridge interaction (VBI) system on bridge frequency extraction. It was found that vehicle frequency higher than the interested bridge frequencies was conducive to bridge frequency extraction. High bridge damping would adversely affect the bridge frequency identification, but the vehicle's damping had little influence on the results. Not only could the vehicle's parameters be modified, but also forced excitation could be applied to the bridge to make its vibrations greater [27]. With active excitation on the bridge, the passing vehicle could collect the bridge's vibration better, and thus the bridge's frequencies could be remarkable in the vehicle's frequency-domain responses. The effect of road roughness is the second negative factor and can pollute bridge frequency identification results. To eliminate the influence of road roughness, Kong et al. [28] proposed subtracting the accelerations of two connected trailers towed by a tractor in the time domain. Compared to using a single vehicle, the residual responses of two trailers were more effective for bridge frequency extraction since the effects of road roughness were weakened. The two connected two-axle vehicles (half-car model) were also verified to be effective in eliminating the influence of track irregularity [29]. However, even though the vehicle's parameters are tuned, the influence of the vehicle cannot be eliminated clearly. Subtracting the rear axle's accelerations from the front axle's accelerations worked poorly for a full-car model [4]. In addition, on-site operation of connected vehicles and tests of two runs with the same trace are hard to be achieved in practice [30].

Using the contact-point (CP) response of the vehicle can help to overcome the above problem related to the vehicle's frequencies. The idea was first employed effectively by a 1-DOF quarter-car model [31]. Later, the idea was tested successfully by a 2-DOF quarter-car [32] and half-car models [33]. Further, the associations between vehicle body and CP responses were investigated using just one sensor when the quarter-car model was employed [34]. Since the displacement at contact points consists of two main resources: the bridge's deflection and road roughness, it has nothing to do with the vehicle itself. Therefore, the vehicle's frequencies are eliminated in the frequency domain. The next step is to suppress the negative effects of road roughness. Similar to the idea of using accelerations, connected vehicles were utilized to remove the influence of road roughness [35]. To circumvent the inconvenience of using connected vehicles in engineering, Yang et al. [36] proposed to remove the vehicle frequencies and road roughness using the residual CP responses of a single vehicle, which was verified effective with a 2-DOF half-car model. He and Yang [30] proposed that the residual acceleration spectrum at contact points of a single two-axle vehicle could be utilized to identify the bridge's frequencies. The first several frequencies of the bridge were successfully extracted under different conditions. The CP response is superior in recognizing the bridge's modal parameters, and it has been utilized in many downstream assignments, such as damage detection [37, 38].

This paper proposes to scan the bridge's frequencies using an instrumented 3D vehicle. For the first time, the CP response of the 3D vehicle, instead of the commonly used quarter- or half-car models, is derived from its accelerations. Tire damping, which is normally ignored in current studies, is extensively included and analyzed when calculating the CP response. Further, considering the practical applications, the position to install accelerometers is the first-ever analyzed in the equations for obtaining the CP response. In order to weaken the influence of road roughness, the residual CP response of the 3D vehicle's wheels is employed. During this process, a novel cross-correlation function-based method is employed instead of the vehicular axle distance measured manually. Several parameters of the VBI system and external influence factors are also discussed for the identification of bridge frequencies.

2. Simulation and CP Response Calculation

2.1. Vehicle Bridge Interaction Model

2.1.1. Vehicle Model. The vehicle model is shown in Figure 1. There are seven DOFs: body bounce z_v, body rocking φ_v, body pitching θ_v, and four wheels' bounces z_{t1}, z_{t2}, z_{t3}, and z_{t4}, which are displayed by red arrows. The parameters of the vehicle are as follows: contact-point displacements: $u_{c1}, u_{c2}, u_{c3}, u_{c4}$; vehicle body mass: m_v; rocking and pitching moment of inertia: $I_{v\varphi}, I_{v\theta}$; constants: a_1, a_2, b_1, b_2; masses of wheels: $m_{t1}, m_{t2}, m_{t3}, m_{t4}$; tires stiffness: $k_{t1}, k_{t2}, k_{t3}, k_{t4}$; tire damping: $c_{t1}, c_{t2}, c_{t3}, c_{t4}$; suspension stiffness: $k_{s1}, k_{s2}, k_{s3}, k_{s4}$; suspension damping: $c_{s1}, c_{s2}, c_{s3}, c_{s4}$; and vehicle speed: v. Dynamic equilibrium equations of vehicle's wheels can be represented by equations (1a)–(1d). By assembling all the vehicle's dynamic equilibrium equations, we can get equation (2), where $\mathbf{M}_v, \mathbf{C}_v$, and $\mathbf{K}_v$ are in Appendix and $\mathbf{p}_{cv}, \mathbf{z}_v$ are shown in equation (3).

$$m_{t1}\ddot{z}_{t1} - c_{s1}\left(\dot{z}_v - \dot{z}_{t1} - b_1\dot{\varphi}_v + a_1\dot{\theta}_v\right) - k_{s1}\left(z_v - z_{t1} - b_1\varphi_v + a_1\theta_v\right) + c_{t1}\left(\dot{z}_{t1} - \dot{u}_{c1}\right) + k_{t1}\left(z_{t1} - u_{c1}\right) = 0, \tag{1a}$$

$$m_{t2}\ddot{z}_{t2} - c_{s2}\left(\dot{z}_v - \dot{z}_{t2} + b_2\dot{\varphi}_v + a_1\dot{\theta}_v\right) - k_{s2}\left(z_v - z_{t2} + b_2\varphi_v + a_1\theta_v\right) + c_{t2}\left(\dot{z}_{t2} - \dot{u}_{c2}\right) + k_{t2}\left(z_{t2} - u_{c2}\right) = 0, \tag{1b}$$

$$m_{t3}\ddot{z}_{t3} - c_{s3}\left(\dot{z}_v - \dot{z}_{t3} - b_1\dot{\varphi}_v - a_2\dot{\theta}_v\right) - k_{s3}\left(z_v - z_{t3} - b_1\varphi_v - a_2\theta_v\right) + c_{t3}\left(\dot{z}_{t3} - \dot{u}_{c3}\right) + k_{t3}\left(z_{t3} - u_{c3}\right) = 0, \tag{1c}$$

$$m_{t4}\ddot{z}_{t4} - c_{s4}\left(\dot{z}_v - \dot{z}_{t4} + b_2\dot{\varphi}_v - a_2\dot{\theta}_v\right) - k_{s4}\left(z_v - z_{t4} + b_2\varphi_v - a_2\theta_v\right) + c_{t4}\left(\dot{z}_{t4} - \dot{u}_{c4}\right) + k_{t4}\left(z_{t4} - u_{c4}\right) = 0, \tag{1d}$$

$$\mathbf{M}_v\{\ddot{\mathbf{z}}_v\} + \mathbf{C}_v\{\dot{\mathbf{z}}_v\} + \mathbf{K}_v\{\mathbf{z}_v\} = \mathbf{p}_{cv}, \tag{2}$$

$$\mathbf{p}_{cv} = \left[0, 0, 0, k_{t1}u_{c1} + c_{t1}\dot{u}_{c1}, k_{t2}u_{c2} + c_{t2}\dot{u}_{c2}, k_{t3}u_{c3} + c_{t3}\dot{u}_{c3}, k_{t4}u_{c4} + c_{t4}\dot{u}_{c4}\right]^T,$$

$$\mathbf{z}_v = \left[z_v, \varphi_v, \theta_v, z_{t1}, z_{t2}, z_{t3}, z_{t4}\right]^T. \tag{3}$$

Here, $u_{ci} = u_{bi} + z_{ri}, \dot{u}_{ci} = \dot{u}_{bi} + \dot{z}_{ri}, i = 1, 2, 3, 4$. u_{bi} is the bridge's deflection at the contact point of i-th wheel. z_{ri} is the road roughness. Initially, the bridge's deflection u_{bi} and velocity $\dot{u}_{bi}$ are assumed as zero. $\dot{z}_{ri}$ can be obtained $\dot{z}_{ri} = vz'_{ri}$, in which $(')$ represents the derivative to x, and x is the distance of the contact point to the bridge's left end.

2.1.2. Bridge Model. The bridge in this study is simulated by N_b Euler–Bernoulli beam element. Two DOFs are considered for each node: vertical transition (Z axis) and rotation on the Y axis, which are shown by blue arrows in Figure 1. The bridge is simply supported at each end. Considering the boundary conditions, there are $N_b + 1$ nodes and $2N_b$ DOFs in total for the bridge. The bridge's dynamic equilibrium equations can be represented in the following equation:

$$\mathbf{M}_b\{\ddot{\mathbf{z}}_b\} + \mathbf{C}_b\{\dot{\mathbf{z}}_b\} + \mathbf{K}_b\{\mathbf{z}_b\} = \mathbf{p}_{b,N}, \tag{4}$$

where $\mathbf{M}_b, \mathbf{C}_b$, and $\mathbf{K}_b$ are the bridge's mass, damping, and stiffness matrices. $\ddot{\mathbf{z}}_b, \dot{\mathbf{z}}_b$, and $\mathbf{z}_b$ are the bridge's acceleration, velocity, and deflection vector, respectively. $\mathbf{p}_{b,N}$ is the nodal load for the bridge, and it is a vector with $2N_b$ entries. The bridge's damping matrix is simulated by the Rayleigh damping assumption, and it can be calculated by $\mathbf{C}_b = a_0\mathbf{M}_b + b_0\mathbf{K}_b$. Since there are two unknown co-efficients, two damping ratios of the first two modes ξ_1 and ξ_2 must be assumed at first and then the global damping matrix $\mathbf{C}_b$ can be obtained. Equations (2) and (4) can be solved by Newmark-β integration method with $\beta = 0.25$ and $\gamma = 0.5$ for unconditional stability.

2.1.3. Interaction Model. Since the vehicle's wheels are not always on the nodes exactly, when the wheel is not on the nodes, the Hermitian cubic interpolation function is employed to distribute the CP force to its two adjacent nodes. For example, in Figure 1, if it is assumed that the first two wheels are on the bridge's fth element and the two rear wheels are on its rth element, the transmission between the CP force and nodal force can be calculated by equations (5)–(7).
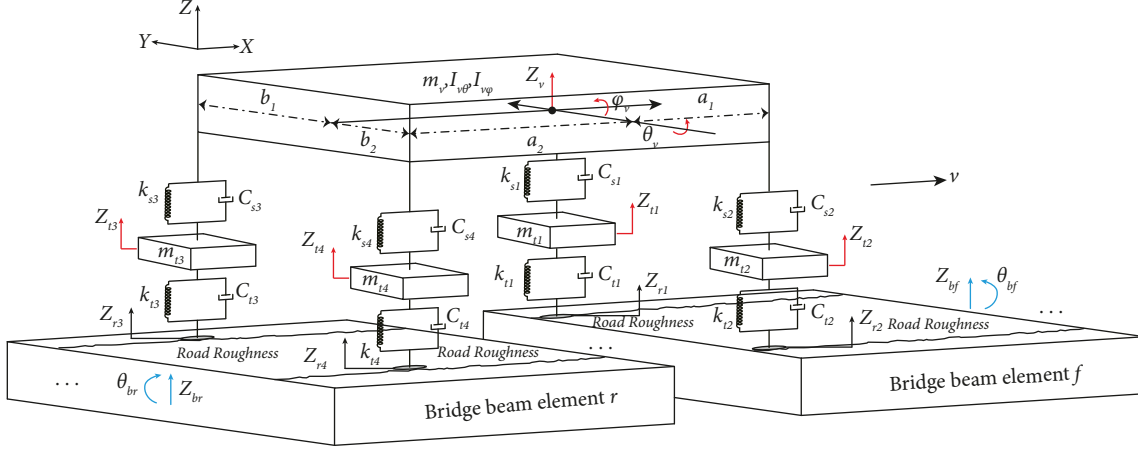
Figure 1: 3D vehicle.

$$\mathbf{p}_{b,N} = \mathbf{N}_c * \mathbf{p}_{cb}, \tag{5}$$

$$\mathbf{N}_c = \begin{bmatrix} 0 & ,\ldots, & 0 & ,\ldots, & \mathbf{N}_f & ,\ldots, & 0 \\ 0 & ,\ldots, & 0 & ,\ldots, & \mathbf{N}_f & ,\ldots, & 0 \\ 0 & ,\ldots, & \mathbf{N}_r & ,\ldots, & 0 & ,\ldots, & 0 \\ 0 & ,\ldots, & \mathbf{N}_r & ,\ldots, & 0 & ,\ldots, & 0 \end{bmatrix}^T_{4 \times 2N_b}, \tag{6}$$

$$\mathbf{N}_f = \begin{bmatrix} 1 - 3\left(\Delta x_f / e_f\right)^2 + 2\left(\Delta x_f / e_f\right)^3 \\ \Delta x_f \left(\Delta x_f / e_f - 1\right)^2 \\ 3\left(\Delta x_f / e_f\right)^2 - 2\left(\Delta x_f / e_f\right)^3 \\ \Delta x_f \left(\left(\Delta x_f / e_f\right)^2 - \left(\Delta x_f / e_f\right)\right) \end{bmatrix}^T_{4 \times 1},$$

$$\mathbf{p}_{cb} = \begin{bmatrix} k_{t1}\left(z_{t1} - u_{c1}\right) + c_{t1}\left(\dot{z}_{t1} - \dot{u}_{c1}\right) \\ k_{t2}\left(z_{t2} - u_{c2}\right) + c_{t2}\left(\dot{z}_{t2} - \dot{u}_{c2}\right) \\ k_{t3}\left(z_{t3} - u_{c3}\right) + c_{t3}\left(\dot{z}_{t3} - \dot{u}_{c3}\right) \\ k_{t4}\left(z_{t4} - u_{c4}\right) + c_{t4}\left(\dot{z}_{t4} - \dot{u}_{c4}\right) \end{bmatrix}_{4 \times 1} - \begin{bmatrix} m_v g \cdot \dfrac{a_2}{\left(a_1 + a_2\right)} \cdot \dfrac{b_2}{\left(b_1 + b_2\right)} + m_{t1}g \\ m_v g \cdot \dfrac{a_2}{\left(a_1 + a_2\right)} \cdot \dfrac{b_1}{\left(b_1 + b_2\right)} + m_{t2}g \\ m_v g \cdot \dfrac{a_1}{\left(a_1 + a_2\right)} \cdot \dfrac{b_2}{\left(b_1 + b_2\right)} + m_{t3}g \\ m_v g \cdot \dfrac{a_1}{\left(a_1 + a_2\right)} \cdot \dfrac{b_1}{\left(b_1 + b_2\right)} + m_{t4}g \end{bmatrix}_{4 \times 1}, \tag{7}$$

where $\mathbf{p}_{cb}$ is the CP force for the bridge. $\Delta x_f(t) = x_f(t) - (f-1)e_f$. e_f is the length of f th element, and $x_f(t)$ is the distance from the wheel's current position at time t to the bridge's left end. Namely, $\Delta x_f(t)$ is the distance between the contact point and the left node of the f th element. Similarly, $\mathbf{N}_r$ can be calculated by replacing f by r in $\mathbf{N}_f$ in equation (6). Employing the Newmark-β integration method again for the bridge, we can get its deflection at contact points represented by $\mathbf{u}_b = \{u_{b1}, u_{b2}, u_{b3}, u_{b4}\}^T = \{\mathbf{N}_c\}^T \mathbf{z}_b$, and the velocity at contact points can be obtained as $\dot{\mathbf{u}}_b = \{\dot{u}_{b1}, \dot{u}_{b2}, \dot{u}_{b3}, \dot{u}_{b4}\}^T = v\{\mathbf{N}_c'\}^T \{\mathbf{z}_b\} + \{\mathbf{N}_c\}^T \dot{\mathbf{z}}_b$. Therefore, equation (3) can be updated, and after that the deflection of the bridge will be updated accordingly. After several iterations, the bridge's

deflection between two adjacent iterations can converge at acceptable values, e.g., 1×10^{-3} mm.

2.2. Road Roughness.

Road roughness has a great influence on bridge frequency identification using the passing vehicle's vibration data. As shown in equation (3), the vehicle is excited by two factors: road roughness and bridge vibrations. Therefore, how to eliminate or weaken the effect of road roughness has been frequently investigated in the last decade [28, 30]. In this study, the road roughness is generated according to ISO 8608 [39]. There are eight classes A–H (from very good to very poor) based on power spectral density (PSD). The process of generating road roughness can

be represented by a normal zero-mean, real-valued stationary Gaussian process, as shown in the following equation:

$$r_{1,3}(x) = \sum_{i=1}^{N} \sqrt{2G_d(n_i)\Delta n} \cos(2\pi n_i x + \theta_{i(1,3)}),$$

$$r_{2,4}(x) = \sum_{i=1}^{N} \sqrt{2G_d(n_i)\Delta n} \cos(2\pi n_i x + \theta_{i(2,4)}),$$ (8)

where $r_{1,3}(x)$ is the road roughness for wheels 1 and 3 and $r_{2,4}(x)$ is for wheels 2 and 4. The difference between these two kinds of road roughness is the random phase angle θ_i that is uniformly distributed in $[0, 2\pi]$. Δn is the interval of spatial frequency and is selected as 0.01 cycle/m in this study. $G_d(n_i)$ is the displacement PSD, and it can be calculated by the following equation:

$$G_d(n_i) = G_d(n_0)\left(\frac{n_i}{n_0}\right)^{-w},$$ (9)

where $G_d(n_0)$ can be properly selected between its lower and upper limit, which can be found in the reference [39] for different road classes. n_i is the spatial frequency, and its lower and upper limits are taken as 0.01 and $10\,\mathrm{m}^{-1}$. The reference spatial frequency n_0 is taken as 0.1 cycle/m, and the fit exponent is assumed as $w = 2$.

2.3. CP Response Calculation. In this study, seven sensors (five translation accelerometers and two angular accelerometers) are utilized to calculate the CP response for the VBI system. The first four translation accelerometers are installed on the axle close to the four wheels, and another one is installed on the vehicle's body. The rest of the two angular accelerometers are installed in the same position as the fifth translation accelerometer. The influence of body sensors' positions will be discussed in Section 4.6. The accelerations will be recorded when the vehicle passes over the bridge. After that, the CP responses can be calculated as follows. In this section, two scenarios are: with or without tire damping, are considered for calculating the CP response.

2.3.1. Tire Damping is Ignored. In many previous studies, the tire's damping was ignored or considered relatively low [4, 40, 41]. It is acceptable if the damping effects of tires are ignored to simplify the calculation of CP responses. By taking the second derivative of equations (1a)–(1d), if $\{c_{ti}, i = 1,2,3,4.\}$ is set as zeros, the CP accelerations of four wheels $\{\ddot{u}_{ci}(t), i = 1,2,3,4.\}$ can be obtained as

$$\ddot{u}_{c1}^{0}(t) = \frac{d^2\ddot{z}_{t1}}{dt^2}\frac{m_{t1}}{k_{t1}} + \ddot{z}_{t1} - \frac{c_{s1}}{k_{t1}}\left(\frac{d\ddot{z}_v}{dt} - \frac{d\ddot{z}_{t1}}{dt} - b_1\frac{d\ddot{\varphi}_v}{dt} + a_1\frac{d\ddot{\theta}_v}{dt}\right) - \frac{k_{s1}}{k_{t1}}\left(\ddot{z}_v - \ddot{z}_{t1} - b_1\ddot{\varphi}_v + a_1\ddot{\theta}_v\right),$$ (10a)

$$\ddot{u}_{c2}^{0}(t) = \frac{d^2\ddot{z}_{t2}}{dt^2}\frac{m_{t2}}{k_{t2}} + \ddot{z}_{t2} - \frac{c_{s2}}{k_{t2}}\left(\frac{d\ddot{z}_v}{dt} - \frac{d\ddot{z}_{t2}}{dt} + b_2\frac{d\ddot{\varphi}_v}{dt} + a_1\frac{d\ddot{\theta}_v}{dt}\right) - \frac{k_{s2}}{k_{t2}}\left(\ddot{z}_v - \ddot{z}_{t2} + b_2\ddot{\varphi}_v + a_1\ddot{\theta}_v\right),$$ (10b)

$$\ddot{u}_{c3}^{0}(t) = \frac{d^2\ddot{z}_{t3}}{dt^2}\frac{m_{t3}}{k_{t3}} + \ddot{z}_{t3} - \frac{c_{s3}}{k_{t3}}\left(\frac{d\ddot{z}_v}{dt} - \frac{d\ddot{z}_{t3}}{dt} - b_1\frac{d\ddot{\varphi}_v}{dt} - a_2\frac{d\ddot{\theta}_v}{dt}\right) - \frac{k_{s3}}{k_{t3}}\left(\ddot{z}_v - \ddot{z}_{t3} - b_1\ddot{\varphi}_v - a_2\ddot{\theta}_v\right),$$ (10c)

$$\ddot{u}_{c4}^{0}(t) = \frac{d^2\ddot{z}_{t4}}{dt^2}\frac{m_{t4}}{k_{t4}} + \ddot{z}_{t4} - \frac{c_{s4}}{k_{t4}}\left(\frac{d\ddot{z}_v}{dt} - \frac{d\ddot{z}_{t4}}{dt} + b_2\frac{d\ddot{\varphi}_v}{dt} - a_2\frac{d\ddot{\theta}_v}{dt}\right) - \frac{k_{s4}}{k_{t4}}\left(\ddot{z}_v - \ddot{z}_{t4} + b_2\ddot{\varphi}_v - a_2\ddot{\theta}_v\right),$$ (10d)

where m_{ti}, k_{ti}, c_{si}, and k_{si} can be tested before the experiment. $\ddot{z}_v$, $\ddot{\varphi}_v$, $\ddot{\theta}_v$, and $\ddot{z}_{ti}$ are accelerations measured in the experiment. a_1, a_2 and b_1, b_2 are constant parameters measured for the vehicle. The zero in the top right corner of $\ddot{u}_{ci}^{0}(t)$ means the zero tire damping scenario. The first-order derivative of the accelerations can be approximately calculated by first-order finite difference formulas, and the second-order of them can be obtained with second-order central formulas as shown in equation (11), where j means the j th sampling point, and Δt is the sampling time interval which can be calculated by $1/f_s$, where f_s is the sampling frequency.

$$\frac{d\ddot{z}_{ti}}{dt} = \frac{\ddot{z}_{ti}(j) - \ddot{z}_{ti}(j-1)}{\Delta t}, \frac{d\ddot{z}_v}{dt} = \frac{\ddot{z}_v(j) - \ddot{z}_v(j-1)}{\Delta t}, \frac{d\ddot{\varphi}_v}{dt} = \frac{\ddot{\varphi}_v(j) - \ddot{\varphi}_v(j-1)}{\Delta t}, \frac{d\ddot{\theta}_v}{dt} = \frac{\ddot{\theta}_v(j) - \ddot{\theta}_v(j-1)}{\Delta t},$$

$$\frac{d^2\ddot{z}_{ti}}{dt^2} = \frac{\ddot{z}_{ti}(j+1) - 2\ddot{z}_{ti}(j) + \ddot{z}_{ti}(j-1)}{(\Delta t)^2}, \quad i = 1,2,3,4; j = 2,3,\ldots.$$ (11)

2.3.2. Tire Damping is Considered. Practical tests have verified that tire damping exists and can influence the vehicle's vibrations [42]. Taking the second derivative of equations (1a)–(1d) and rearranging items about $\ddot{u}_{ci}$, we can get equations (12) and (13), in which we use d at the top right corner of $\ddot{u}_{ci}^d(t)$ to represent the scenario when tire damping is considered. From equation (13), we can understand that if c_{ti}/k_{ti} is relatively small (e.g., $< 10^{-3}$ s), the first item in

equation (13) $c_{ti}/k_{ti} \cdot d\ddot{u}_{ci}^d(t)/dt$ will contribute little for the final results of $\ddot{u}_{ci}^d(t)$, and thus it can be ignored. Then, we can get $\ddot{u}_{ci}^d(t) \approx Q_i(t)$. However, when the ratio of the tire's damping to stiffness c_{ti}/k_{ti} is relatively high (e.g., $> 10^{-3}$ s), the first item in equation (13) cannot be ignored. By solving the first-order linear differential equations and assuming that the CP responses start at zero at $t = 0$, equation (14) can be obtained for four wheels.

$$Q_i(t) = \ddot{u}_{ci}^0(t) + c_{ti}\frac{d\ddot{z}_{ti}}{dt}, \quad i = 1, 2, 3, 4, \tag{12}$$

$$\frac{c_{ti}}{k_{ti}}\frac{d\ddot{u}_{ci}^d(t)}{dt} + \ddot{u}_{ci}^d(t) = Q_i(t), \quad i = 1, 2, 3, 4, \tag{13}$$

$$\ddot{u}_{ci}^d(t) = \frac{k_{ti}}{c_{ti}}e^{-k_{ti}/c_{ti}t}\left[\int_0^t Q_i(\tau)e^{k_{ti}/c_{ti}\tau}d\tau\right], \quad i = 1, 2, 3, 4. \tag{14}$$

In engineering, accelerations are sampled by sensors in discrete format, so the integration item in equation (14) cannot be obtained directly. The integration is transformed into numerical summation with respect to the time, as shown in the following equation:

$$\ddot{u}_{ci}^d(t) = \frac{k_{ti}}{c_{ti}}\left[\sum_{j=1}^{t/\Delta t}\left(Q_i|_j\right)e^{k_{ti}/c_{ti}(j\Delta t - t)}\Delta t\right], \quad i = 1, 2, 3, 4; j = 1, 2, \ldots, \tag{15}$$

where Δt is the sampling time interval the same as before and j means the jth sampling point of accelerations. $Q_i|_j$ is calculated at the jth point using equation (12). In this study, the simplest rectangular numerical integration method is utilized. Midpoint, Trapezoid, or Simpson's rule can be utilized to improve the precision of numerical integration.

3. Simulation Results and Discussion

3.1. Simulation. This section discusses a case study based on the analysis in Section 2. The vehicle and bridge's parameters can be found in Table 1. All symbols are the same as introduced before. The sampling time interval for both the vehicle and the bridge is set as 0.001 s ($f_s = 1000$ Hz). The vehicle and the bridge are assumed motionless at the beginning (zero displacements, zero velocity, and zero acceleration), and the contact responses for four wheels are set as zeros when $t = 0$.

For the vehicle, its frequencies are denoted by $f_{v1} - f_{v7}$ in Table 1. Tire damping of the vehicle is from the reference [4], and other parameters are collected from a car in the reference [43]. The vehicle's axle distance and width are 2.87 m and 1.45 m, respectively. Due to the uneven weights on the vehicle, the gravity center is not in the geometrical center of the vehicle body but is eccentrically located. Namely, $a_1, a_2, b_1,$ and b_2 are mutually different. The gravity center of the vehicle body is difficult to be located in practice. The influence of errors in locating the gravity center will be discussed later in Section 4.6.

For the bridge, it is simply supported at each end with a span length of 25 m. It is divided into 10 elements, and each element's length is 2.5 m. The FE model of the bridge is shown in Figure 2. All parameters of the bridge are collected from the reference [44]. With the above parameters, the bridge's first three frequencies can be obtained, as shown in Table 1. The bridge's damping is temporarily assumed as zero and will be considered in Section 4.5. During the passage of the vehicle, only the points under the four tires are excited and other bridge elements will vibrate freely. To obtain the second frequency of the bridge, the accelerometer installed on the bridge is on its left half span to collect the bridge's vibration data.

For the road roughness, in this section, A class (very good) with $G_d(n_0) = 4 \times 10^{-6}$ m^3 road is utilized for the comparison to the "no roughness" scenario. The influence of different road roughness classes will be discussed in Section 4.1. The two left wheels are assumed to pass on the same road roughness, and the right two wheels will pass on the same roughness as well but different from the left roughness. Road roughness for left and right wheels is shown in Figures 3(a) and 3(c).

According to Yang et al. [36], a key influence of using a generated road profile is that the vehicle's wheel will not experience the zigzag road roughness point by point. There is a contact area between the tire and the bridge. A commonly employed way to handle this effect is to use the smoothed road profile. In this study, it is assumed that the contact length of the vehicle's tire and the bridge is 0.04 m. Namely, a 0.04 m (0.04/5/0.001 = 8 sampling points) moving average filter (MAF) is used to smooth the original road roughness. The smoothed road roughness is represented by the red dotted line in Figures 3(a) and 3(c), and the PSD of them is plotted in Figures 3(b) and 3(d). It can be seen that the generated road roughness can fit the A-class road in IOS 8608 very well, and the road roughness for left wheels and right wheels are different. Therefore, the vehicle passing the road will have pitching and rocking vibrations at the same time.

TABLE 1: Parameters of the vehicle and bridge.

VBI	Vehicle parameters	Values
Vehicle	m_v	1085 kg
	$I_{v\varphi}$	$1100 \, \text{kg} \cdot \text{m}^2$
	$I_{v\theta}$	$820 \, \text{kg} \cdot \text{m}^2$
	$m_{t1}, m_{t2}, m_{t3}, m_{t4}$	40, 40, 40, 40 kg
	$c_{s1}, c_{s2}, c_{s3}, c_{s4}$	$2 \times 10^3, 2 \times 10^3, 2 \times 10^3, 2 \times 10^3 \, \text{N} \cdot \text{s/m}$
	$c_{t1}, c_{t2}, c_{t3}, c_{t4}$	$430, 430, 430, 430 \, \text{N} \cdot \text{s/m}$
	$k_{s1}, k_{s2}, k_{s3}, k_{s4}$	$1 \times 10^4, 1 \times 10^4, 1 \times 10^4, 1 \times 10^4 \, \text{N/m}$
	$k_{t1}, k_{t2}, k_{t3}, k_{t4}$	$1.5 \times 10^5, 1.5 \times 10^5, 1.5 \times 10^5, 1.5 \times 10^5 \, \text{N/m}$
	a_1, a_2, b_1, b_2	1.4, 1.47, 0.7, 0.75 m
	Speed v	5 m/s (18 km/h)
	Vehicle frequencies $f_{v1} - f_{v7}$	0.673, 0.935, 1.551, 10.066, 10.067, 10.069, 10.074 Hz
Bridge	Length l_b	25 m
	Young's modulus E	27.5 GPa
	Moment of inertia I_b	$0.2 \, \text{m}^4$
	Mass per unit length $\overline{m}$	2400 kg/m
	Bridge frequencies $f_{b1} - f_{b3}$	3.805, 15.220, 34.260 Hz
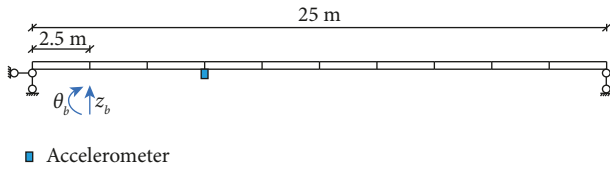
FIGURE 2: FE model of the bridge.

3.2. Results and Discussion

3.2.1. No Road Roughness. When no road roughness is considered, the vehicle body's vibrations and frequency-domain responses can be found in Figure 4. Because there is no road roughness, the left and right wheels will experience just the bridge's deflection. Since the vehicle's gravity center is not in the geometrical center of its body, the pitching and rocking effects occur simultaneously. But it can be seen that the rocking angular accelerations are much smaller than the pitching and bounce responses, and they are not on the same scale. Figure 4(b) plots the normalized amplitudes of the vehicle body's accelerations. It can be observed that the bridge's first two frequencies (only 0–20 Hz responses are plotted because 20–50 Hz responses are very weak and near zero) can be identified, but the second bridge frequency is relatively weak. The vehicle's first three frequencies are noticeable in the frequency domain. Figures 4(c) and 4(d) plot the vertical accelerations of the vehicle's four wheels. It can be seen that the vehicle's vertical vibrations are similar to the free vibrations of a single degree of freedom structure when it passes on the bridge. Because there is no road roughness, the front two wheels' vibrations are nearly the same, and so are the rear two wheels. This is because the excitation for four wheels comes from the deflection of the bridge only. From normalized amplitudes, we can see that in the frequency domain, the bridge's first three frequencies can be found, but the third one is relatively weak.

Figure 5 plots the vibration data of the bridge. From Figure 5, it can be seen that the bridge's vibration is periodical. Its first three frequencies can be clearly found using the vibrations recorded by the sensor installed on the bridge.

No vehicle frequency peaks are found. Similar to the vehicle's frequency-domain responses, the amplitude at the bridge's third frequency is relatively low.

The results for calculating the CP responses of wheel 2 are shown in Figure 6. It can be seen from Figure 6(a) that the calculated CP responses (using equation (15)) are nearly the same as the true CP responses. Here, the true CP responses mean the ones obtained by using the road profile and the bridge's deflection directly because these two are already known in simulation. However, in practical engineering, the road roughness and the bridge's deflection are not known; they must be calculated indirectly using equations (10), (12), or (15). The high overlapping between the true and calculated CP responses of wheel 2 verifies that the derived equations are correct. It can be seen from Figure 6(b) that the bridge's first three frequencies can be clearly identified when wheel 2's CP responses are utilized without the interference of vehicle frequencies. Note that when wheels 1, 3, and 4 are employed to obtain the according CP responses, the normalized amplitudes can also indicate the bridge's first three frequencies. To save the length of this paper, they are not plotted here. The back-calculated CP responses can be good references for extracting the bridge's frequencies. Also, it should be noted that because of the shifting effect of the vehicle's moving speed, the bridge's frequencies extracted from CP responses will be split into two frequencies: $f_{bn} - n\pi v/l_b$ and $f_{bn} + n\pi v/l_b$, which can be also observed in references [26, 36].

By the analysis above, it can be clearly seen that the vehicle's vibration data not only include the modes of it but also contain the bridge's dynamic information. By comparison of Figures 4 and 6, we can find that the vehicle's frequencies have been totally filtered out when the wheel's CP responses rather than its accelerations are employed, making the bridge's frequencies highlighted and more visible.

3.2.2. With Road Roughness: A-Class. Road roughness is a crucial factor inversely influencing the bridge frequency extraction from the vehicle's vibration data. In this section, the A-class road roughness generated in Section 3.1 will be
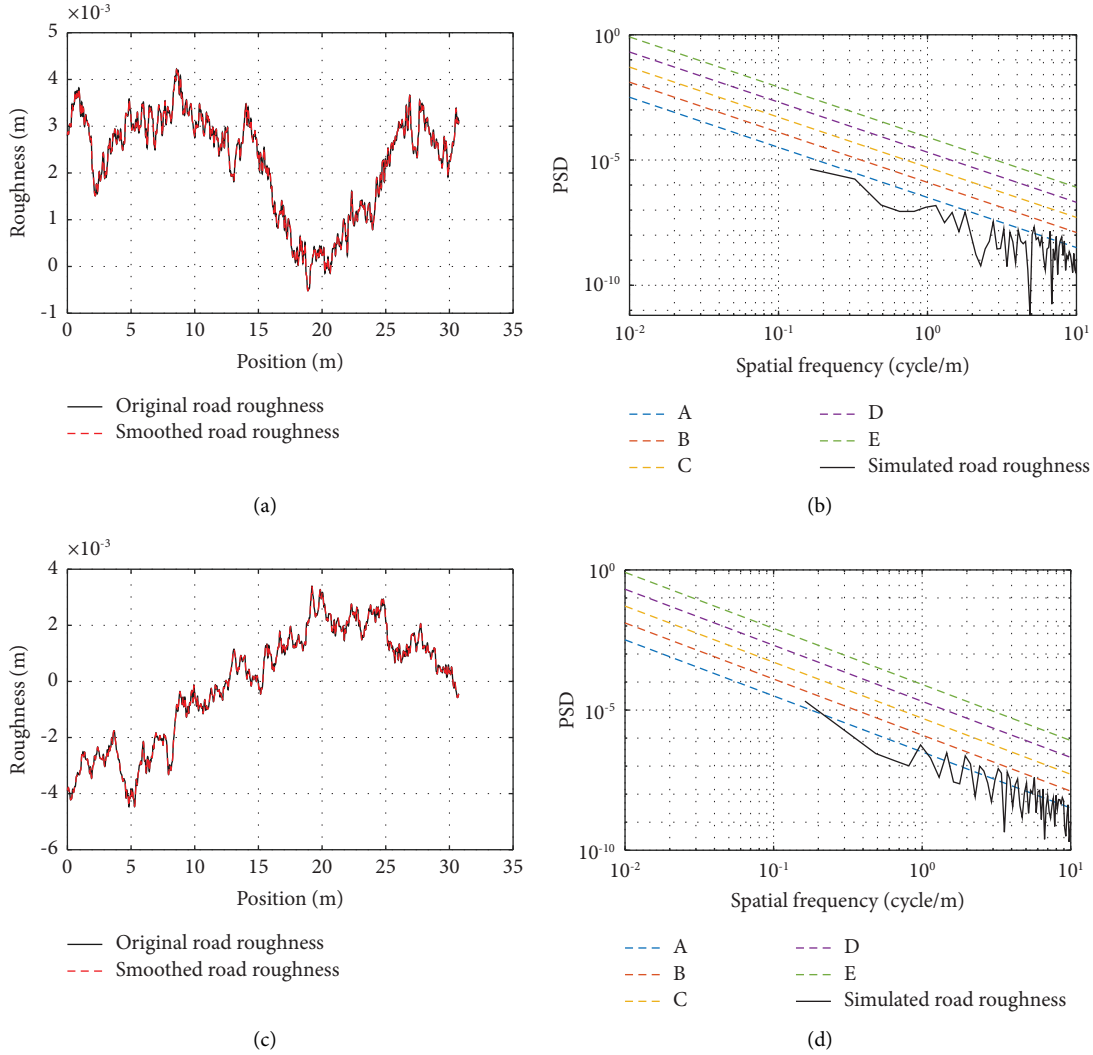
(a)

(b)

(c)

(d)

FIGURE 3: Road roughness: (a) Road roughness for left wheels. (b) PSD of road roughness for left wheels. (c) Road roughness for right wheels. (d) PSD of road roughness for right wheels.

utilized. The simulation results of the vehicle's acceleration are shown in Figure 7. We can see that due to the influence of the road roughness, the vehicle's acceleration amplitude is much greater. It can be seen from Figure 7(a) that due to the road roughness under four wheels, the vehicle body's accelerations have been on the nearly same scale, meaning the success of simulation for different road roughness for the vehicle's two left wheels and two right wheels. Different from the scenario of no road roughness discussed in Section 3.2.1, in Figure 7(b), the bridge's first two frequencies cannot be identified anymore. Figures 7(c) and 7(d) plot the accelerations of the vehicle's wheels. It can be seen that the wheels' accelerations are quite complex. In its frequency-domain responses, the bridge's frequencies have been submerged in the amplitudes. Most peaks locate near vehicle's $f_{v4} - f_{v7}$ and the bridge frequencies cannot be picked out accurately.

For the bridge, it can be seen from Figure 8 that it is excited greater owing to the road roughness. The first three frequencies can be identified better than the scenario of no road roughness. Also, it can be observed that the acceleration magnitude of the bridge (-0.05 to $0.05 \, \text{m/s}^2$) is smaller than that of the vehicle's wheels (-3.0 to $3.0 \, \text{m/s}^2$).

Similarly, CP responses of wheel 2 can also be calculated with good precision using equation (15), as shown in Figure 9(a). To present the accuracy of back-calculated CP responses, the mean absolute error (MAE) is calculated using equation (16), where $\hat{y}_t$ represents the calculated CP responses and y_t means the ground truth. The MAE value can be obtained as $0.797 \, \text{m/s}^2$. Considering the scale of CP response is $[-10, 10]$, such errors will not cause large deviations when identifying bridge frequencies using calculated CP responses. However, even though the CP responses calculation is precise, the bridge's frequencies cannot be identified in the frequency domain anymore. Most peaks in the frequency domain are about the road roughness that is generated randomly. Therefore, we can understand that in the frequency domain of a single wheel's accelerations or CP responses, the bridge's frequencies will be overshadowed by the influence of road roughness.
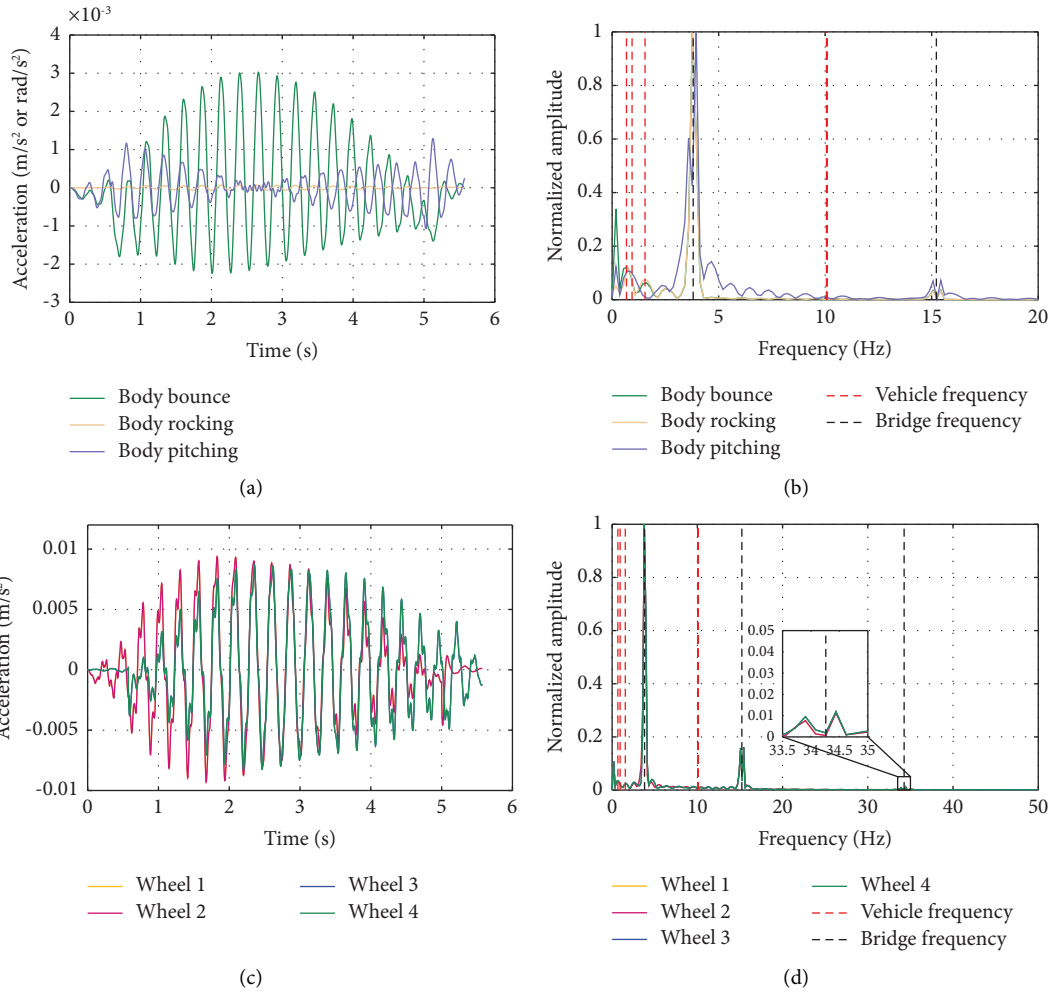
Figure 4: Vehicle's vibrations and FFT amplitude: no road roughness. (a) Vehicle's rocking and pitching acceleration. (b) |FFT| of rocking and pitching acceleration. (c) Vehicle's body and wheels' acceleration. (d) |FFT| of body and wheels' acceleration.
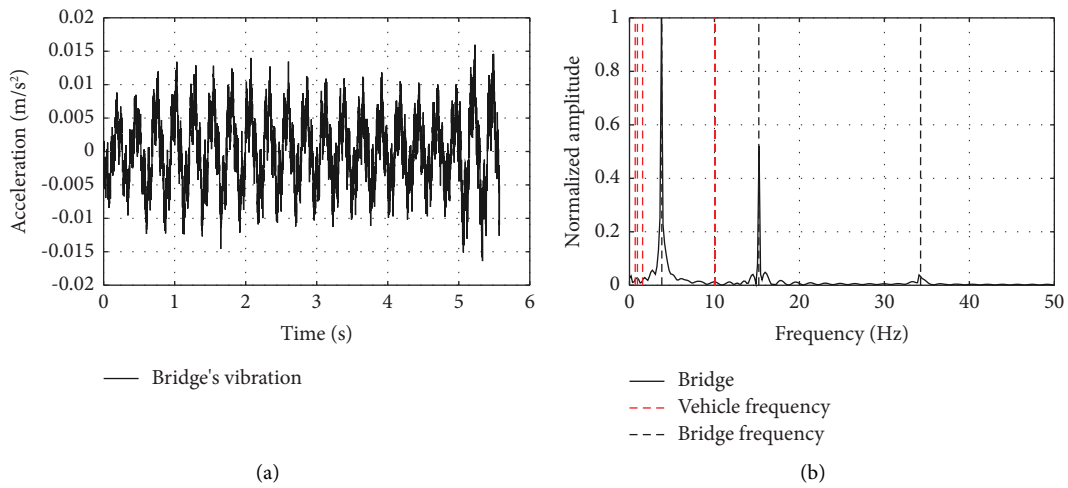

Figure 5: Bridge acceleration and FFT amplitude: no road roughness. (a) Bridge's acceleration. (b) |FFT| of bridge's acceleration.
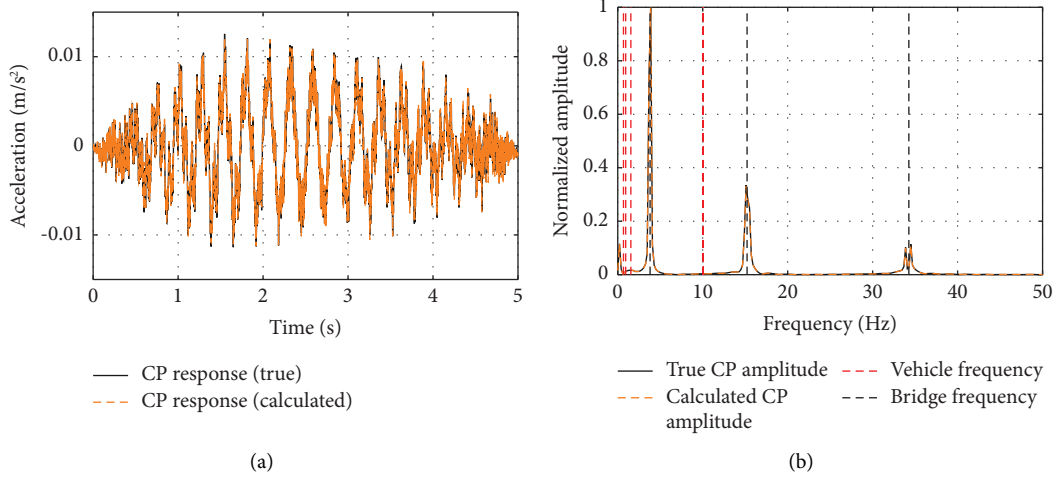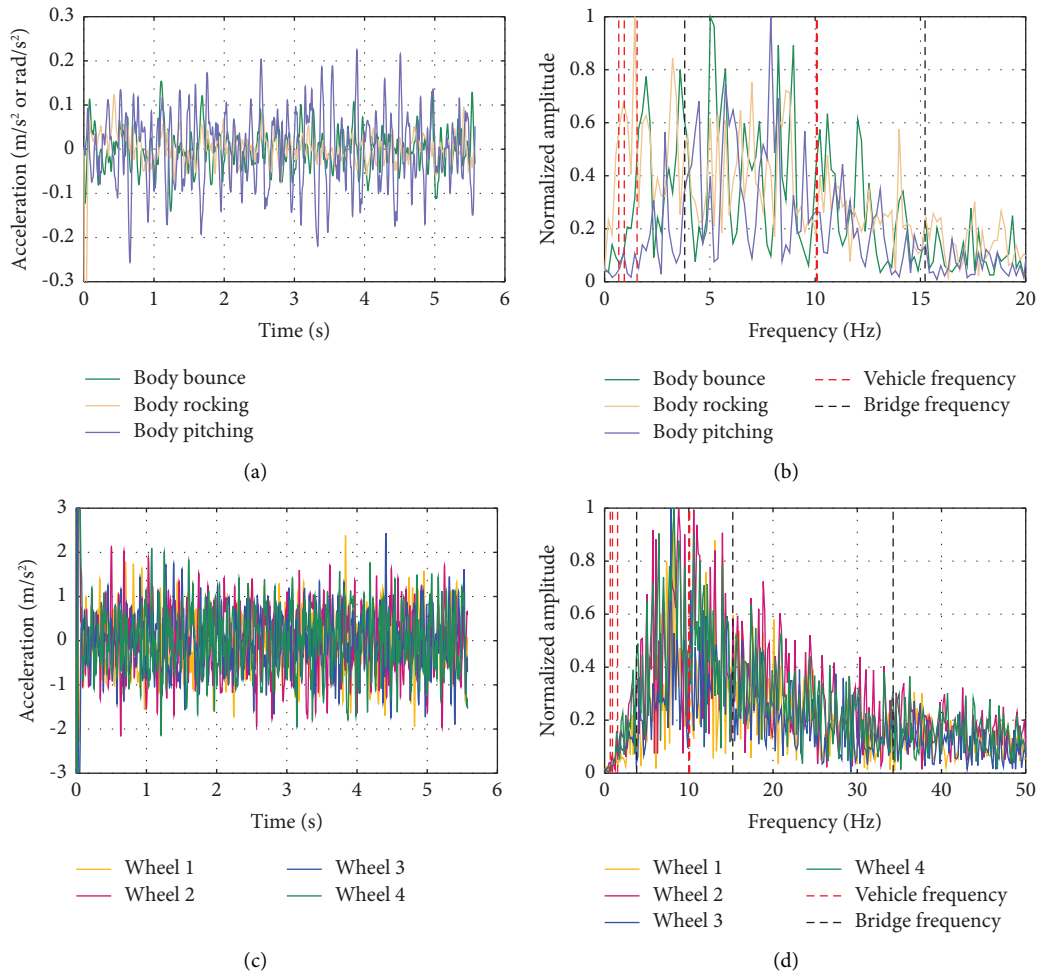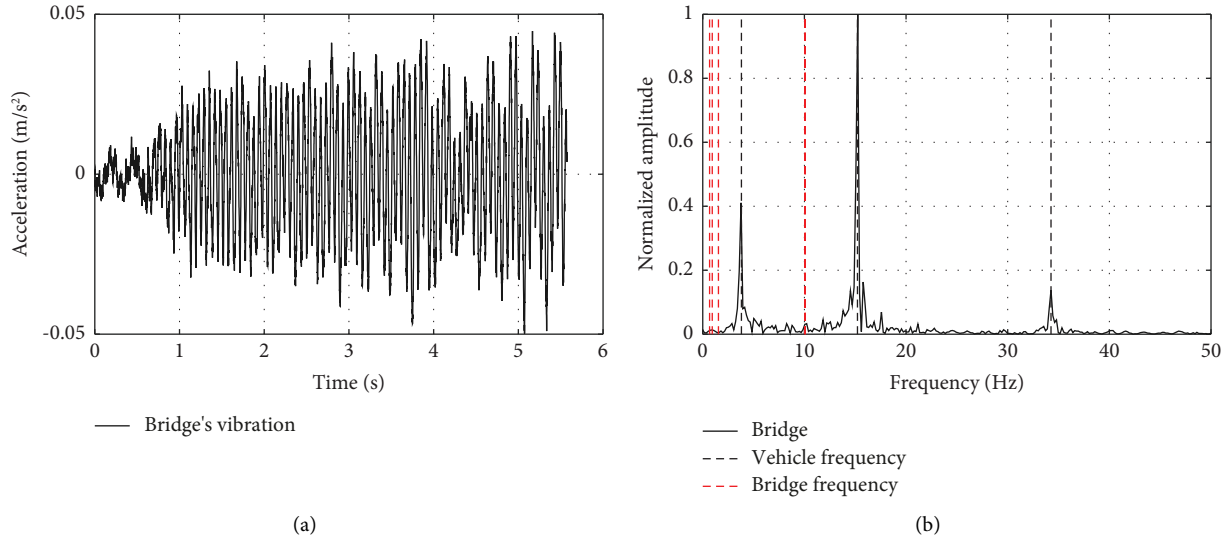
(a)

(b)

FIGURE 6: CP response of wheel 2 and FFT amplitude: no road roughness. (a) CP responses of wheel 2. (b) |FFT| of wheel 2's CP responses.

(a)

(b)

(c)

(d)

FIGURE 7: Vehicle's vibrations and FFT amplitude: A-class road roughness. (a) Vehicle's rocking and pitching acceleration. (b) |FFT| of rocking and pitching acceleration. (c) Vehicle's body and wheels' acceleration. (d) |FFT| of body and wheels' acceleration.

$$\text{MAE} = \frac{1}{N} \sum_{t=1}^{N} |\widehat{y}_t - y_t|. \qquad (16)$$

To solve the above problem caused by road roughness, the residual CP responses can be utilized. Compared to reference employing connected vehicles, this study utilizes only one 3D

FIGURE 8: Bridge acceleration and FFT amplitude: A-class road roughness. (a) Bridge's acceleration. (b) |FFT| of bridge's acceleration.
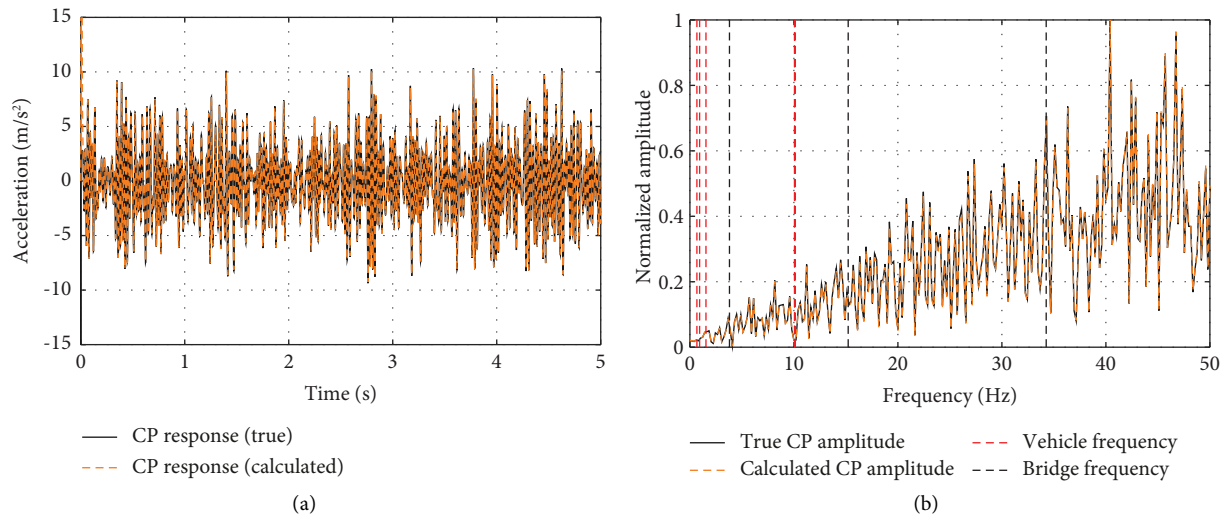

FIGURE 9: CP response of wheel 2 and FFT amplitude: A-class road roughness. (a) CP responses of wheel 2. (b) |FFT| of wheel 2's CP responses.

vehicle passing the bridge. Since it has been proved that the vehicle's frequencies can be removed by utilizing the CP responses in Section 3.2.1, if the road roughness influence can be eliminated, the bridge's frequencies can be extracted better. Wheels on the same side of the vehicle will experience the same road roughness with a time lag (the vehicle is assumed to run in a straight line), so the CP responses of them will be partially the same when they pass the same road roughness point. Actually, the CP responses contain two parts: the acceleration caused by road roughness and the bridge's deflection. When two wheels pass the same position on the bridge, the only difference between their CP responses is the component caused by the bridge's deflection. Therefore, by subtracting the rear wheel's CP responses (wheels 3 and 4) from the front wheel's CP responses (wheels 1 and 2) at the same place on the bridge, the road roughness effects can be

eliminated. The residual CP responses' normalized amplitudes in the frequency domain are plotted in Figure 10. The time lag can be represented by sampling point interval (SPI), which denotes how many sampling points should be shifted from the front wheel's signals. In engineering, the SPI can be calculated by the distance between the front and rear axle ($l_v = a_1 + a_2$), vehicle speed v, and the sampling frequency f_s by SPI = $l_v/v \cdot f_s$. However, it is hard to measure l_v precisely in a practical application. The influence of SPI and the solution to obtain it will be introduced in Section 4.7.

Figure 10 plots the identified bridge's frequencies using the residual CP responses of wheels 1 and 3 and wheels 2 and 4. We can see that the calculated residual CP response amplitudes can match real amplitudes very well, indicating that the CP response calculation using equation (15) can meet good precision. Also, it can be found that using the
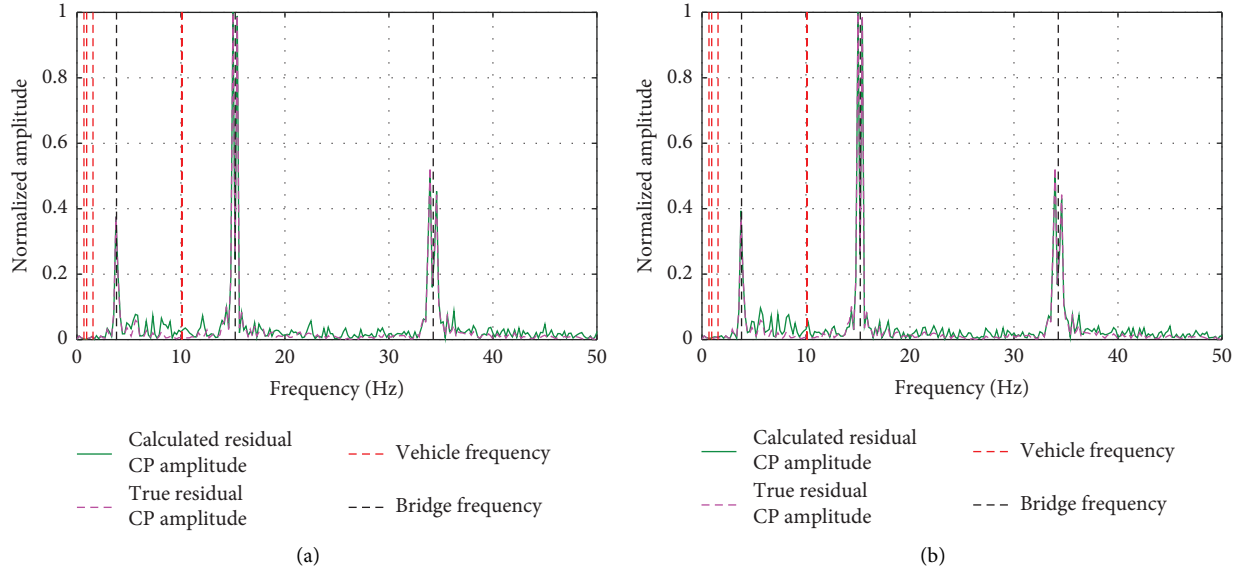
FIGURE 10: Normalized residual CP amplitude of the vehicle. (a) Residual CP amplitude using wheels 1 and 3. (b) Residual CP amplitude using wheels 2 and 4.

residual responses of wheels 1 and 3 (left wheels) or 2 and 4 (right wheels) can both identify the bridge's first three frequencies without the pollution of the vehicle's frequencies. Compared to the amplitude in Figure 6 when no road roughness is considered, using the residual CP responses makes the bridge's third frequency highlighted.

4. Parametric Study

Before applying the proposed method in engineering, the flexibility must be tested under different conditions. Since both wheels 1and 3 and wheels 2 and 4 can identify the bridge's frequencies, in the following content, only normalized residual CP amplitudes using wheels 1 and 3 are displayed. Unless special statement, the parameters are the same as Section 3.2.2.

4.1. Road Roughness. In Section 3.2, extraction of the bridge's frequencies with no road roughness and A-class road roughness is discussed. However, in practical engineering, the bridge's road class is unknown. In this section, the road classes B $(G_d(n_0) = 32 \times 10^{-6} \mathrm{m}^3)$, C $(G_d(n_0) = 128 \times 10^{-6} \mathrm{m}^3)$, D $(G_d(n_0) = 512 \times 10^{-6} \mathrm{m}^3)$, and E $(G_d(n_0) = 2048 \times 10^{-6} \mathrm{m}^3)$ will be investigated. It is assumed that the bridge's road surface is under the same class, meaning that the scenario that two left wheels and two right wheels experience different class road roughness is impossible. With the same parameters in Section 3.2 and road roughness of different classes, Figure 11 can be obtained.

We can see from Figure 11 that because the road roughness has been eliminated from the residual CP responses, different classes of road roughness do not have an obvious influence on the extraction of the bridge's frequencies. Also, it can be seen that the peaks of the first three bridge frequencies are different. This is because the

road roughness is generated randomly. The moving forces applied to the bridge will be different due to the random roughness. Therefore, which frequency will be the highest is also random. Similarly, it can be found that each bridge's frequency is also split into two frequencies, just like in Figure 10.

4.2. Vehicle Speed. Vehicle speed is one of the most important factors influencing the extraction of the bridge's frequencies from the vehicle's accelerations. High speed will typically increase the excitation amplitude induced by the vehicle so that the bridge will be excited greater. This is conducive to transferring the bridge's dynamic information to the vehicle. In comparison, if the vehicle's speed is low, the vehicle will move only a little distance in a sampling interval, and the road roughness will vary very little. Thus, the excitation is relatively smaller, and thus both the vehicle and bridge will be excited just slightly, which may not be enough for bridge frequency identification. However, very high speed will make the vehicle's passing time too short to be analyzed. The vehicle cannot collect sufficient data, thus limiting the bridge's dynamic information in the vehicle's accelerations. Hence, selecting a proper vehicle speed is of great importance before applying the VSM.

In Section 3, the vehicle at 5 m/s speed is discussed. In this section, another four vehicle speeds, 2.5, 7.5, 15, and 30 m/s (representing 9, 27, 54, and 108 km/h in actual cases), are considered when extracting the bridge's frequencies from residual CP responses. The bridge frequency identification results are shown in Figure 12.

From Figure 12, we can see that when the speed is relatively low (see 2.5 m/s) because the vehicle's passing time is long, the frequency resolution is high. However, as the speed is low, the bridge is not fully excited. It can be found
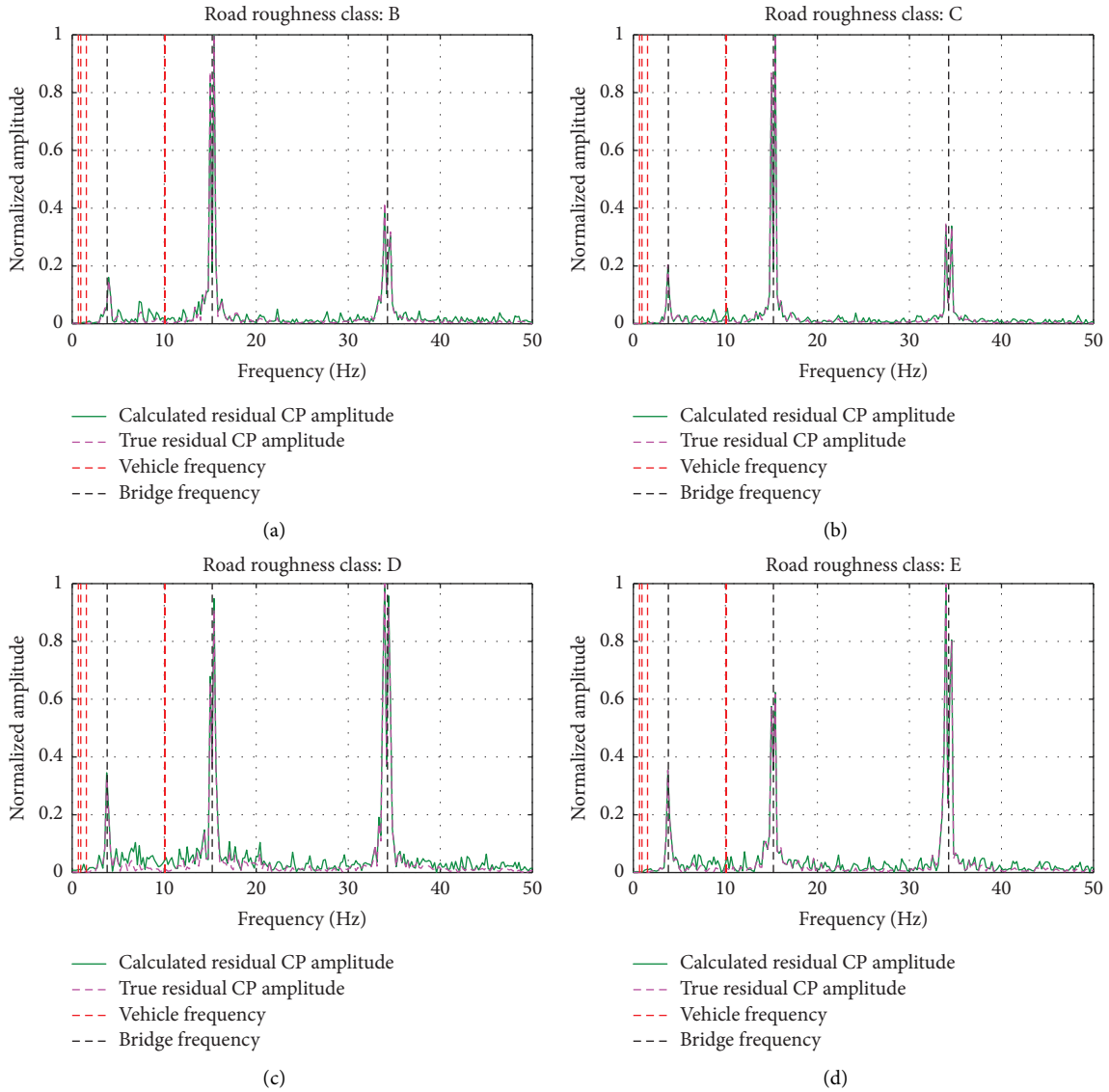
FIGURE 11: Normalized residual CP amplitude: different road roughness classes. (a) Normalized residual CP amplitude: class *B*. (b) Normalized residual CP amplitude: class *C*. (c) Normalized residual CP amplitude: class *D*. (d) Normalized residual CP amplitude: class *E*.

from Figure 12(a) that the bridge's first three frequencies can be identified, but the third one is very weak. After the speed increases to 7.5 m/s or 15 m/s, it can be noticed that the first three frequencies of the bridge can be extracted very well. At the same time, we can see that the frequency resolution gradually decreases, and the width of the frequency peaks becomes wider. When the speed reaches 30 m/s (highway speed), the vehicle's passing time will become only 1.025 s. The identified frequency spectrum becomes quite poor. But the bridge's first three frequencies can still be outstanding, which demonstrates the effectiveness of the proposed method. It is also worth noting that after the vehicle speed increases the phenomenon that the bridge's frequency is split into two frequencies: $f_{bn} - n\pi v/l_b$ and $f_{bn} + n\pi v/l_b$ are more noticeable. This result matches findings in references when quarter- or half-car models are utilized [26, 45].

4.3. Vehicle Tire Damping.
The transmission of dynamic information between the bridge and vehicle is accomplished via four tires. When calculating the CP responses, the tire's damping is a key factor influencing which equations will be utilized (e.g., zero damping: equation (10), little damping: equation (12), and high damping: equation (15)). Compared with Section 3, in this section, two additional scenarios will be discussed: zero damping and high damping. The high damping is simulated by increasing the tire damping $c_{t1}, c_{t2}, c_{t3}, c_{t4}$ in Table 1 by ten times, namely, 4500 N · s/m.

Figure 13 plots the comparison between the true and calculated CP responses of wheel 2 using different equations under different scenarios. To make lines more distinguishable, only responses within the first 1 s are displayed. When no tire damping is considered, as shown in Figure 13(a), we can see that the CP responses of wheel 2 can
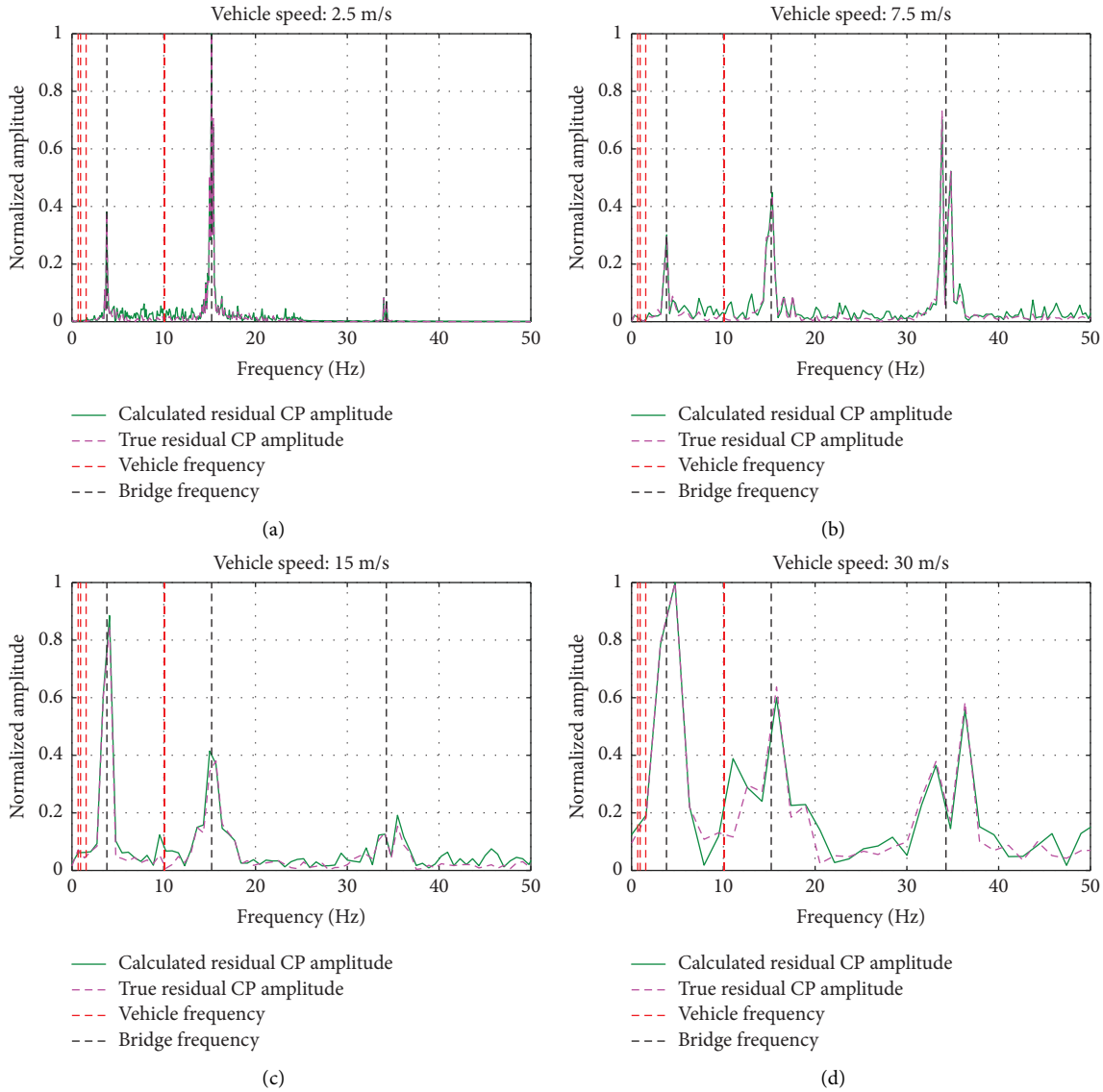
Figure 12: Normalized residual CP amplitude: different vehicle speeds. (a) Normalized residual CP amplitude: 2.5 m/s. (b) Normalized residual CP amplitude: 7.5 m/s. (c) Normalized residual CP amplitude: 15 m/s. (d) Normalized residual CP amplitude: 30 m/s.

be calculated with good precision using equation (10). Accordingly, the extracted normalized residual CP amplitude is plotted by the green line in Figure 13(d). It can be seen that the bridge's first three frequencies are successfully identified. When high tire damping is considered, the CP response estimation using equation (12) does not work, as shown in Figure 13(b). Obvious errors can be noticed between true and calculated CP responses. This is because the first item in equation (13) cannot be ignored under this condition. To obtain the CP responses accurately, equation (15) is employed, and the results are shown in Figure 13(c). It can be seen that for the high damping scenario, CP responses can be obtained precisely. But at the beginning, due to the entry of the front wheels and high damping, some differential errors are noticed. Utilizing calculated CP responses with high tire damping, the bridge's first three frequencies

are obtained, as shown by the yellow line in Figure 13(d). We can see that the bridge's first three frequencies can still be clearly identified.

Also, it can be seen that the calculated CP responses of wheel 2 with and without damping are much similar (see Figures 13(a) and 13(c)). To investigate the reason for this observed phenomenon, the bridge's deflections under the front and rear CP points are plotted in Figure 14. In fact, the displacement at CP points includes two parts: the road roughness and the bridge's deflection. The road roughness is the same for both zero and high damping scenarios. For the bridge's deflection, from Figure 14, we can see that the bridge's deflection under the front CP point is much similar, and only a slight difference (see the red line and blue dotted line) can be observed. So is the bridge's deflection under the rear CP point (see the yellow line and brown dotted line).
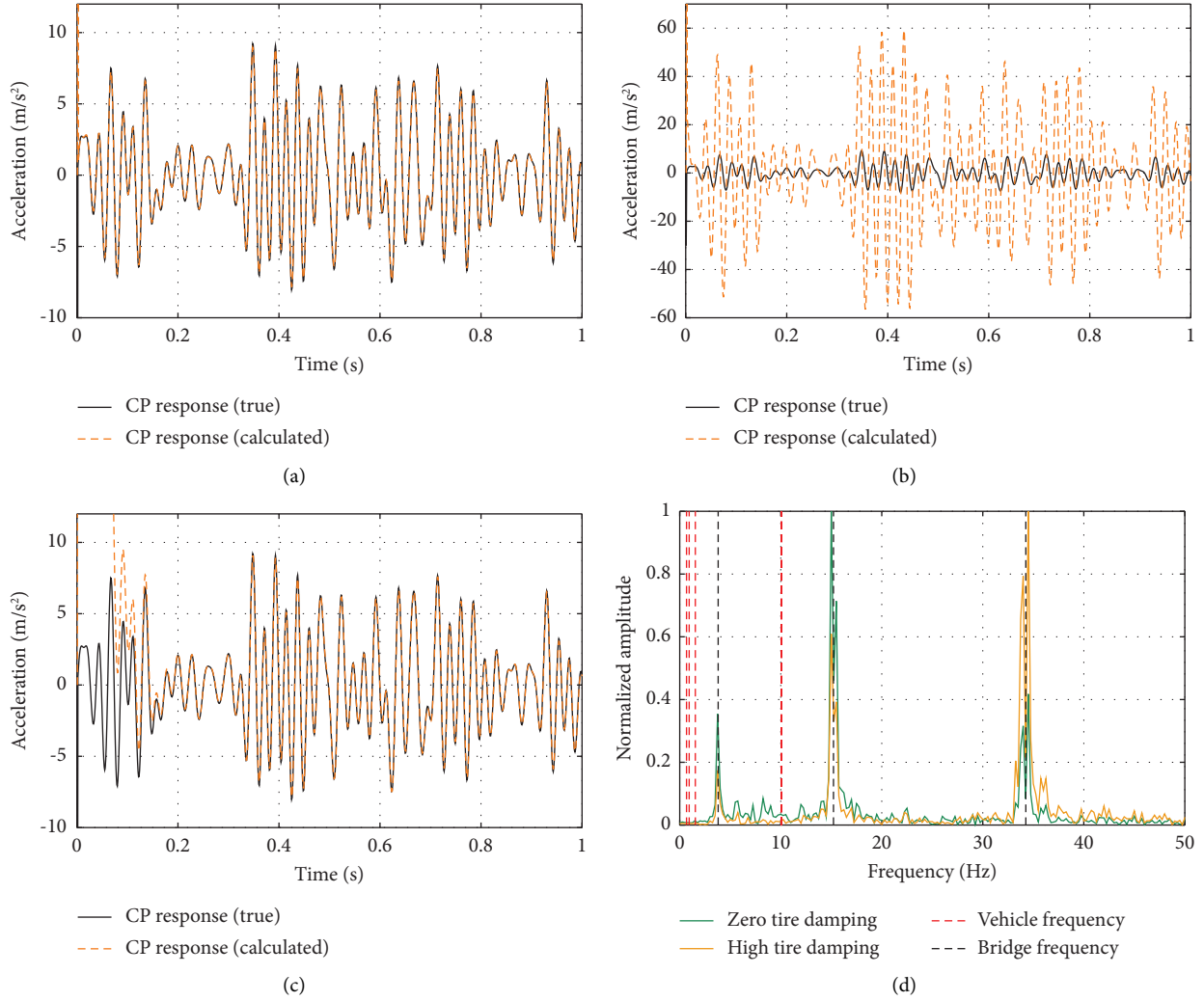
FIGURE 13: Calculated CP responses and residual amplitude using different tire damping (wheel 2). (a) CP responses: zero damping, using equation (10). (b) CP responses: high damping, using equation (12). (c) CP responses: high damping, using equation (15). (d) Residual CP amplitude: zero and high damping.

This can explain the above phenomena that the CP responses are similar, whether the damping is zero or high. Therefore, the above analysis indicates that the vehicle's tire damping has little influence on the extraction of the bridge's frequencies when CP responses are employed.

4.4. Noise Level. In engineering, environmental and measurement system noises are inevitable. Generally, the noise level is between 1% and 10% [4, 36]. In this section, the influence of different environmental noise levels 1%, 3%, 5%, and 7% are considered. All measured accelerations of the vehicle will be contaminated by simulated noises. The process of adding noises can be finished by the following equation [46]:

$$\mathbf{x}_{\text{noise}} = \mathbf{x} + n_l \cdot \sqrt{\|\mathbf{x}\|_2/n_x} \cdot \text{randn}(n_x), \qquad (17)$$

where $\mathbf{x}$ is a vector representing the acceleration of the vehicle in one DOF and n_x is its length. n_l is the noise level, and it is 0.01, 0.03, 0.05, or 0.07 herein. $\text{randn}(n_x)$ is

a function that can generate an n_x-dimension vector including entries that are independently drawn from the standard normal distribution. All other parameters are the same as in Section 3.2.2. An example of adding 5% noise to the acceleration of wheel 2 is shown in Figure 15(a). Accordingly, utilizing equation (15), its CP responses can be obtained as shown in Figure 15(b). We can see that due to the influence of noises, the calculated CP responses cannot match the real CP responses very well. Under different noise levels, the results of identifying the bridge's frequencies are shown in Figure 16.

It can be seen from Figure 16 that when the noise level is relatively low (see 1% noise), even though the calculated CP responses cannot match true CP responses very well, the bridge's first three frequencies can still be clearly identified. With the increase in noise level (see 3% noise), the bridge's third frequency is partially submerged by noisy peaks. Compared with Figure 10(a) when no noise is introduced, identification of the bridge's first two frequencies is also influenced. After the noise level increases to 5% and 7%, the
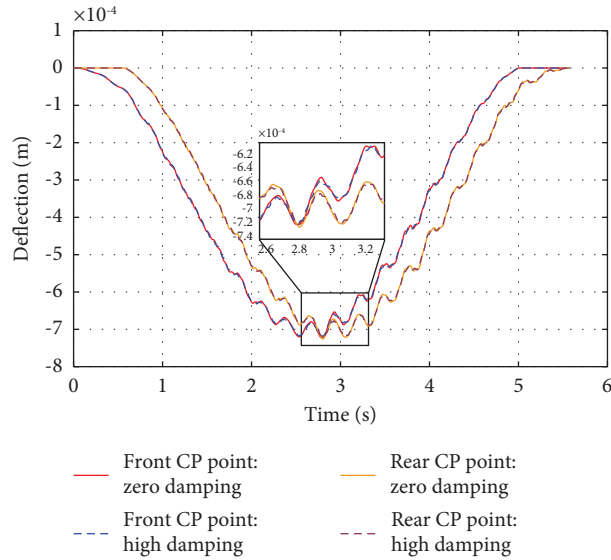
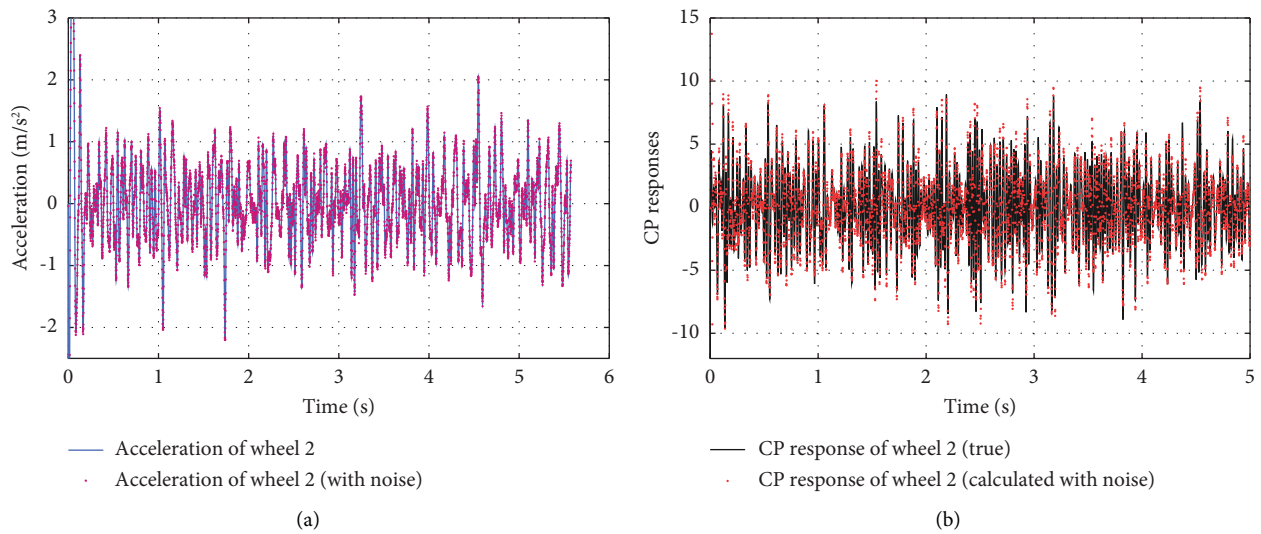FIGURE 14: Bridge's deflection under front and rear CP points.

(a)

(b)

FIGURE 15: Accelerations and CP responses of wheel 2: with noise. (a) Accelerations of wheel 2: with or without noise. (b) CP responses of wheel 2: true and with noise.

third frequency is totally overshadowed by the noise. However, the adverse noise effects only occur in the relatively high-frequency range (>20 Hz), and the first two frequencies are still identifiable.

From the aforementioned analysis, we can see that the environmental noises are negative for the extraction of the bridge's frequencies from CP responses. This is because the environmental noises are random and cannot be removed by residual CP responses. Fortunately, in practical engineering, the noise frequencies are normally in the high-frequency range, and the bridge's frequencies are low, making the proposed method more applicable in engineering. To improve the performance of the proposed method, a low-pass filter can be utilized to alleviate the inverse effects of noises.

4.5. Bridge Damping.

As discussed in Section 2, the bridge's damping ratio is simulated by Rayleigh damping, in which two order damping ratios need to be determined at first. In this section, two scenarios: $\xi_1 = \xi_2 = 1\%$ and $\xi_1 = \xi_2 = 2\%$ are used to calculate the damping matrix of the bridge $\mathbf{C}_b$. Other parameters are the same as in Section 3.2.2. The bridge frequency identification results are shown in Figure 17.

It can be seen from Figure 17 that when the damping ratio is relatively low, the bridge's first three frequencies can be identified very well, but peaks around the bridge's frequencies become more complex after the bridge's first two order damping ratios increase to 2%. It can be seen that peaks at both the second and third frequencies are suppressed. Bridges with high damping will negatively influence
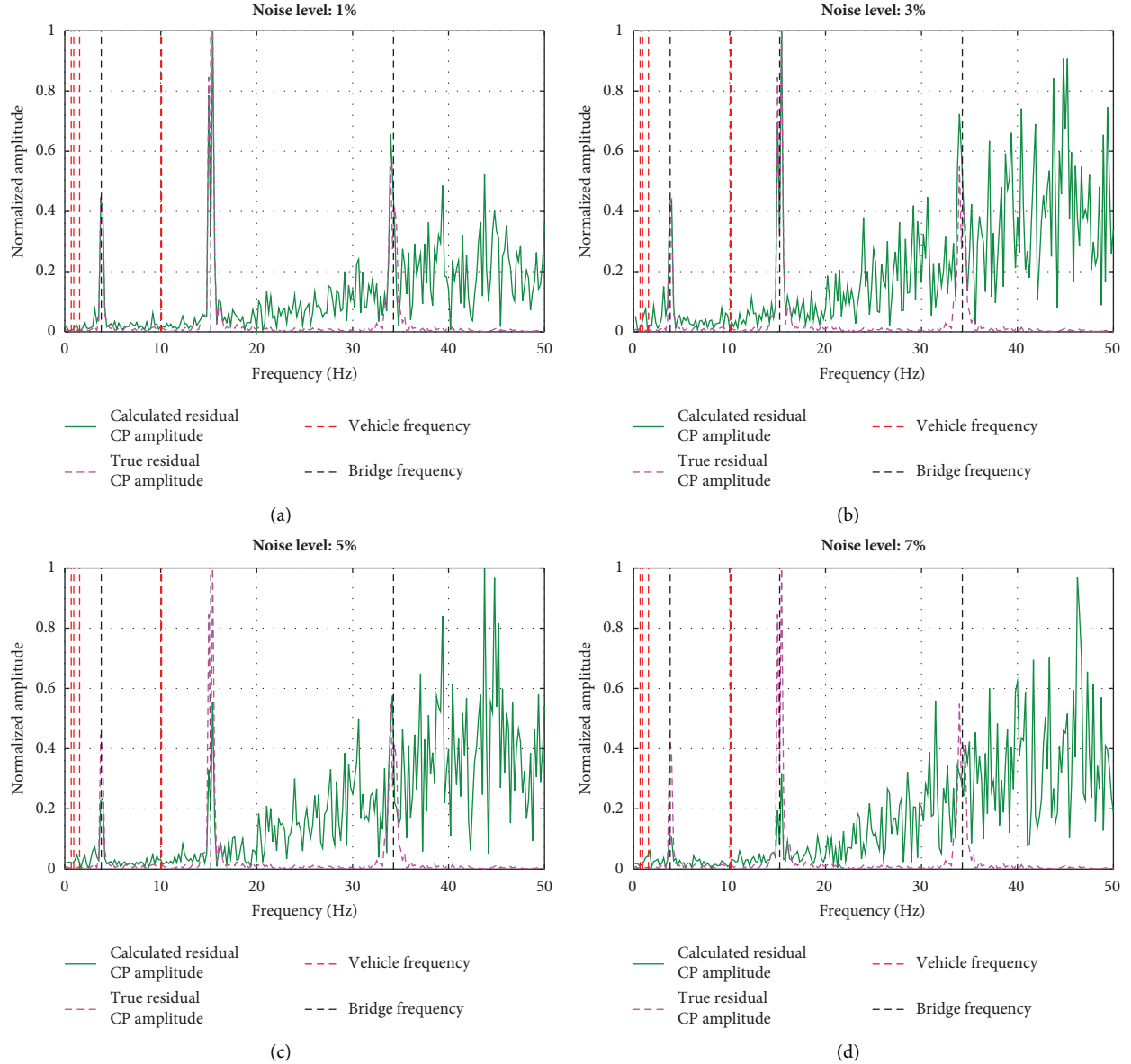
FIGURE 16: Normalized residual CP amplitude: different noise levels. (a) Normalized residual CP amplitude: 1% noise. (b) Normalized residual CP amplitude: 3% noise. (c) Normalized residual CP amplitude: 5% noise. (d) Normalized residual CP amplitude: 7% noise.

the transmission of their dynamics to the vehicle. Moreover, when the bridge's damping is high, its vibrations will be restrained as well, which makes CP responses include less bridge information.

4.6. Body Sensor Position. When calculating the CP responses for a wheel using equations (10), (12), or (15), $\{k_{si}, c_{si}, k_{ti}, c_{ti}, m_{ti}, i = 1,2,3,4.\}$ and $m_v, I_{v\varphi}, I_{v\theta}$ can be measured and updated by on-site tests. The positions of four accelerometers measuring wheels' accelerations can be referred to $S_5 - S_8$ in reference [42]. As the vehicle's body in this study is assumed to be rigid, the positions of two angular accelerometers measuring $\ddot{\varphi}_v$ and $\ddot{\theta}_v$ on the vehicle's body

have no influence on the collected angular accelerations. However, for the body's translation accelerometer, requiring it to be installed on the gravity center exactly is too strict since the gravity center cannot be captured without professional equipment. This section will investigate the influence of the vehicle body sensor position on backcalculated CP responses.

To investigate the positional influence of the body's translation accelerometer, Figure 18 shows a sensor position (the red point) that is different from the gravity center (the black point). When the vertical accelerations of the vehicle body are measured, the constants for the vehicle body will be changed accordingly, as shown in the following equation:

Bridge's first two order damping ratio: 1%

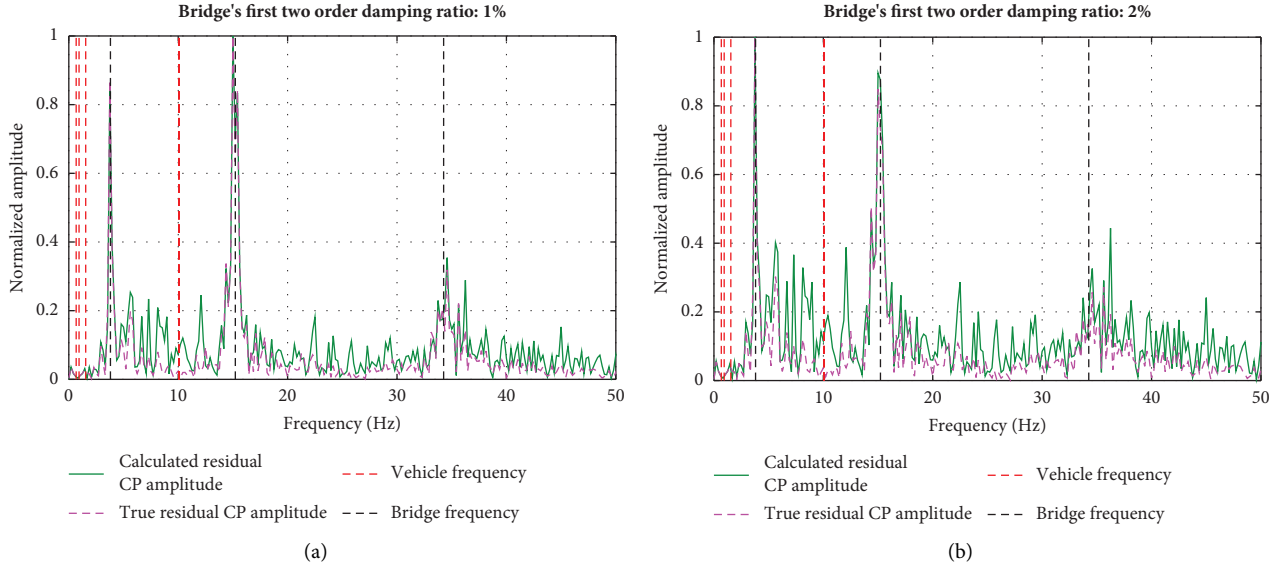**Bridge's first two order damping ratio: 2%**

(a)

(b)

FIGURE 17: Normalized residual CP amplitude: different bridge damping. (a) First two order damping ratio: 1%. (b) First two order damping ratio: 2%.
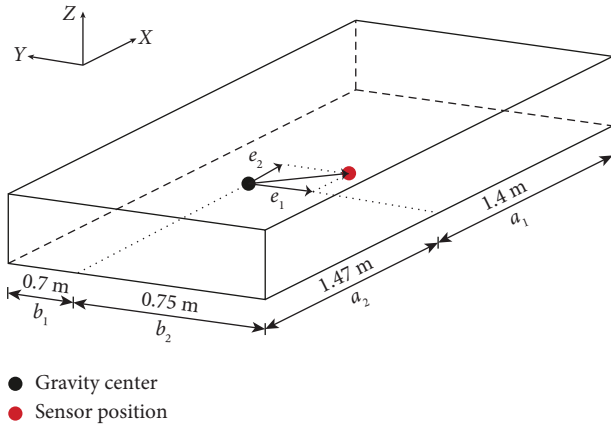

FIGURE 18: Sensor is not installed on the gravity center.

$$\widetilde{a}_1 = a_1 - e_2; \widetilde{a}_2 = a_2 + e_2; \widetilde{b}_1 = b_1 + e_1; \widetilde{b}_2 = b_2 - e_1, \quad (18)$$

where $\widetilde{a}_1, \widetilde{a}_2, \widetilde{b}_1, \widetilde{b}_2$ are new constants for the vehicle body when the sensor is not put on the gravity center exactly. a_1, a_2, b_1, b_2 are the original constants for locating the gravity center. At the same time, even though the angular accelerations collected on the new position are the same as the gravity center, the vertical acceleration will be impacted by the sensor position. The updated vehicle body's vertical acceleration can be calculated by the following equation:

$$\widetilde{\ddot{z}}_v = \ddot{z}_v + e_1\ddot{\varphi}_v + e_2\ddot{\theta}_v, \quad (19)$$

where $\ddot{z}_v$ is the acceleration of the vehicle body's gravity center which cannot be directly measured in practice. $\widetilde{\ddot{z}}_v$ is the acceleration measured on the new sensor position. By replacing $\ddot{z}_v, a_1, a_2, b_1, b_2$ by $\widetilde{\ddot{z}}_v, \widetilde{a}_1, \widetilde{a}_2, \widetilde{b}_1, \widetilde{b}_2$ in equation (12), we can notice that values of $Q_i(t)$ will not be changed, and

the influence of errors on sensor position has been eliminated in equation (12). Since $Q_i(t)$ is not changed and equation (15) is just related to k_{ti}, c_{ti}, and $Q_i(t)$. The calculated CP responses will not change. In other words, the body translation sensor's position will not influence the results of calculated CP responses as long as $\widetilde{a}_1, \widetilde{a}_2, \widetilde{b}_1, \widetilde{b}_2$ are carefully measured to locate the sensor's position on the vehicle body.

The aforementioned analysis is based on the assumption that the vehicle body is absolutely rigid. In practice, the vehicle body may deform slightly due to the excitation transmitted from the suspension system. This may render some errors in measuring the vehicle body's vertical or angular accelerations. Thus, the authors would recommend that (1) angular accelerometers should be installed close to the body's translation accelerometer and (2) the position of three body accelerometers are suggested to be installed as close as possible to the gravity center so as to eliminate the inverse effects on the body's deformation.

4.7. Sampling Point Interval. In the last sections, the distance between the front and rear axle must be precisely measured so that the SPI between the front and rear wheels can be obtained when used to subtract CP responses of the rear wheel (e.g., wheel 3) from the front wheel (e.g., wheel 1). However, precise measurement of the distance between two wheels will be impossible due to the measurement precision. To solve the above problem in engineering, in this study, the cross-correlation function (CCF) of the front and rear wheels' CP responses is utilized to measure the value of SPI. As discussed previously, the displacement at CP points contains two parts: the road roughness and the bridge's deflection. The bridge's vibrations are normally submerged by the road's roughness, as shown in Figure 9(b).
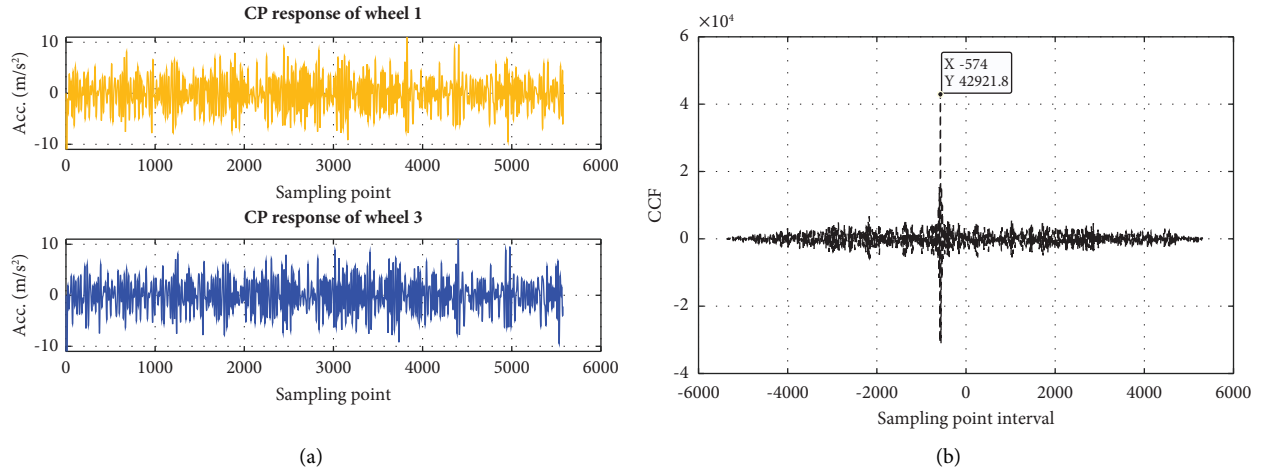
FIGURE 19: CP responses and CCF value for wheels 1 and 3. (a) CP responses of wheels 1 and 3. (b) CCF values with respect to SPI value.
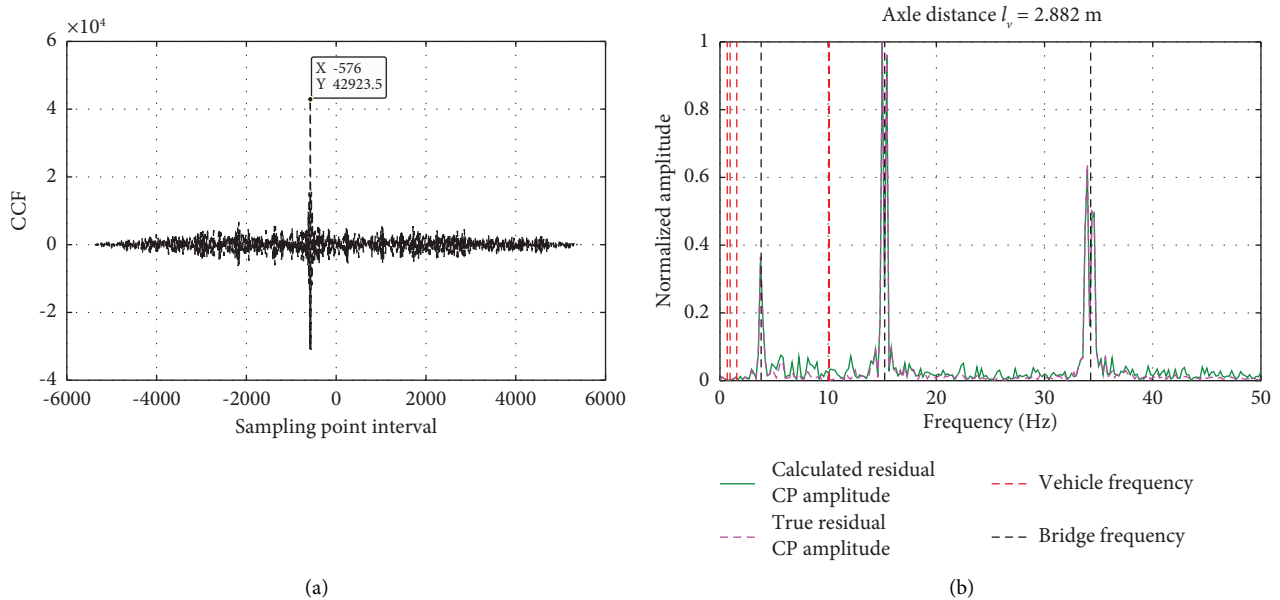

FIGURE 20: SPI calculation and normalized residual CP amplitude: $l_v = 2.882$ m. (a) CCF values with respect to SPI value. (b) Normalized residual CP amplitude.

Notwithstanding, the above characteristics can also provide an idea for calculating the distance between the front and rear wheels. By calculating the CCF value of CP responses of front and rear wheels, how many sampling points should be shifted from the front wheel's CP responses can be obtained, namely, the SPI value. The basic principle of the proposed method is that when the front and rear wheels experience the same point of road roughness, their CP responses will be highly related since the response caused by road roughness plays a main role in the CP responses. A similar method has been investigated by reference [4] where the front and rear wheels' accelerations are employed. To improve the proposed method, CP responses are utilized in this study. Using CCF values of CP responses, no measurement of axle distance is needed, thus avoiding the error of measurement. Since this study utilized

the CP responses rather than the vehicle's accelerations, compared to the reference [4], interference of vehicle's frequencies is avoided.

Figure 19(a) shows the CP response of wheels 1 and 3. By calculating their CCF, Figure 19(b) can be obtained. It can be seen that when the distance between two axles is $l_v = 2.87$ m and the sampling frequency is $f_s = 1000$ Hz, the $SPI = -574$ is obtained between wheels 1 and 3. This result matches the method $SPI = l_v/v \cdot f_s$ mentioned in Section 3.2.2. Utilizing the determined SPI value, the residual CP responses of wheels 1 and 3 are obtained. Their normalized residual CP amplitude can be calculated by FFT, which is exactly the same as Figure 10(a). Employing the above method, the distance between two axles l_v does not need to be measured manually, thus avoiding the error introduced by artificial measurement.

Another potential problem is that, in practice, the measurement precision of the distance between front and rear axles is generally in millimeter-level (not decimeter-level). For example, if the exact distance of two wheels is $l_v = 2.882$ m ($a_1 = 1.4$ m and $a_2 = 1.482$ m) and the vehicle speed is $v = 5$ m/s, the minimum sampling distance interval is 5 mm. This means that when the rear wheel passes the same roughness as the front wheel passes, due to the limitation of the sampling frequency, the corresponding acceleration is not recorded at that roughness point. Utilizing the proposed CCF-based method, it can be calculated as $SPI = -576$, as shown in Figure 20(a) (the true value should be $SPI = 2.882/5 \times 1000 = 576.4$). Therefore, there is a $0.4 \times 5/1000 = 0.002$ m error between the calculated axle distance and the true one. Employing the SPI value -576 calculated by CCF and repeating the same process for wheels 1 and 3, we can obtain Figure 20(b).

It can be seen from Figure 20(b) that the bridge's first three frequencies are also captured even though there is a 2 mm error in axle distance measurement; such a minor error will not cause large divergences in identifying the bridge's frequencies since the road roughness does not change very sharply in such a small distance. Thus, the effectiveness of the CCF-based method is verified and can be applied in engineering. If more accurate results are expected, the authors recommend that the sampling frequency be improved so that residual CP responses can be calculated more accurately.

5. Conclusions and Future Work

This paper proposes a promising method to extract the bridge's several frequencies from the vehicle's acceleration data. To extract the bridge's frequencies accurately and efficiently, the residual CP responses between the front and rear wheels are employed. The major negative influence of road roughness is suppressed, and the vehicle frequencies are eliminated by the proposed method, making the bridge's frequencies more noticeable. To test the robustness of the proposed method, several factors, including vehicle parameters, environmental noises, bridge damping, and measurement errors, are considered. Several concluding remarks are drawn in the following:

(1) A 3D vehicle with seven DOFs is established to simulate a real car with four wheels, and the equations for calculating CP responses using a full-car model's vibrations are derived. The vehicle wheel's CP responses calculated by the derived equations are vehicle frequency-free, making the bridge frequencies highlighted and easily recognized.

(2) The road roughness is a key factor that pollutes the results of bridge frequency extraction from the vehicle's vibration. For a full-car model, the bridge's frequencies cannot be directly identified by accelerations or CP responses. Instead, residual CP responses of front and rear wheels can be utilized to eliminate the negative effects of road roughness, and the bridge frequencies can be extracted clearly.

(3) The 3D vehicle body's rocking, pitching, and vertical vibrations are relatively low compared to the wheel's vibration amplitude (around 1/10 in this study). Even though they cannot be utilized directly to identify the bridge's frequencies, they play a role in calculating CP responses for each tire.

(4) Robustness of the proposed method is verified under different road roughness classes, vehicle speeds, tire damping, noise levels, and bridge damping. Among the above influence factors, road roughness classes and tire damping have little influence on the bridge frequency identification results. High vehicle speed makes the frequency resolution low but bridge frequencies are still identifiable. Environmental noises can negatively affect bridge frequency identification in the high-frequency range (>20 Hz in this study). High bridge damping restrains the transmission of the bridge's dynamic information to the vehicle and thus has inverse effects on identifying bridge frequencies.

(5) Considering practical applications of the proposed method, two on-site measurement factors are investigated: vehicle body sensor position and SPI. It is shown that the errors introduced by vehicle body sensor position can be eliminated when calculating the CP responses for tires, thus will not influence bridge frequency identification results. A novel method to obtain the SPI is utilized, which circumvents errors introduced by manually measuring axle distance and is thus more applicable in engineering.

Even though encouraging results are obtained utilizing the instrumented vehicle and the beam bridge model and several influence factors are investigated on scanning the bridge frequencies, more realistic VBI models, including 3D bridge and 3D road roughness, need to be further explored. In addition, the effects of other factors, such as vehicle engine influence, ongoing traffic loads, temperature effects, and vehicular model updating errors, are also important and deserve deep investigations. Our future study will be extended to check more sophisticated models and the influence of the above factors and verify the effectiveness of the proposed method in field tests.

Appendix

A. Matrices of the Vehicle

$$
\mathbf{M}_v = \begin{pmatrix} \mathbf{M}_{v1} & 0 \\ 0 & \mathbf{M}_{v2} \end{pmatrix}, \mathbf{M}_{v1} = \begin{pmatrix} m_v & 0 & 0 \\ 0 & I_{v\varphi} & 0 \\ 0 & 0 & I_{v\theta} \end{pmatrix}, \mathbf{M}_{v2} = \begin{pmatrix} m_{t1} & 0 & 0 & 0 \\ 0 & m_{t2} & 0 & 0 \\ 0 & 0 & m_{t3} & 0 \\ 0 & 0 & 0 & m_{t4} \end{pmatrix},
$$

$$
\mathbf{C}_v = \begin{pmatrix} \mathbf{C}_{v11} & \mathbf{C}_{v12} \\ \mathbf{C}_{v21} & \mathbf{C}_{v22} \end{pmatrix}, \mathbf{K}_v = \begin{pmatrix} \mathbf{K}_{v11} & \mathbf{K}_{v12} \\ \mathbf{K}_{v21} & \mathbf{K}_{v22} \end{pmatrix},
$$

$$
\mathbf{C}_{v11} = \begin{pmatrix} c_{s1}+c_{s2}+c_{s3}+c_{s4} & -b_1(c_{s1}+c_{s3})+b_2(c_{s2}+c_{s4}) & -a_2(c_{s3}+c_{s4})+a_1(c_{s1}+c_{s2}) \\ -b_1(c_{s1}+c_{s3})+b_2(c_{s2}+c_{s4}) & b_1^2(c_{s1}+c_{s3})+b_2^2(c_{s2}+c_{s4}) & a_1b_2c_{s2}-a_1b_1c_{s1}+a_2b_1c_{s3}-a_2b_2c_{s4} \\ -a_2(c_{s3}+c_{s4})+a_1(c_{s1}+c_{s2}) & a_1b_2c_{s2}-a_1b_1c_{s1}+a_2b_1c_{s3}-a_2b_2c_{s4} & a_1^2(c_{s1}+c_{s2})+a_2^2(c_{s3}+c_{s4}) \end{pmatrix},
$$

$$
\mathbf{C}_{v12} = \begin{pmatrix} -c_{s1} & -c_{s2} & -c_{s3} & -c_{s4} \\ b_1c_{s1} & -b_2c_{s2} & b_1c_{s3} & -b_2c_{s4} \\ -a_1c_{s1} & -a_1c_{s2} & a_2c_{s3} & a_2c_{s4} \end{pmatrix}, \mathbf{C}_{v21} = \begin{pmatrix} -c_{s1} & b_1c_{s1} & -a_1c_{s1} \\ -c_{s2} & -b_2c_{s2} & -a_1c_{s2} \\ -c_{s3} & b_1c_{s3} & a_2c_{s3} \\ -c_{s4} & -b_2c_{s4} & a_2c_{s4} \end{pmatrix},
$$

$$
\mathbf{C}_{v22} = \begin{pmatrix} c_{s1}+c_{t1} & 0 & 0 & 0 \\ 0 & c_{s2}+c_{t2} & 0 & 0 \\ 0 & 0 & c_{s3}+c_{t3} & 0 \\ 0 & 0 & 0 & c_{s4}+c_{t4} \end{pmatrix}, \mathbf{K}_{v22} = \begin{pmatrix} k_{s1}+k_{t1} & 0 & 0 & 0 \\ 0 & k_{s2}+k_{t2} & 0 & 0 \\ 0 & 0 & k_{s3}+k_{t3} & 0 \\ 0 & 0 & 0 & k_{s4}+k_{t4} \end{pmatrix},
$$

$$
\mathbf{K}_{v11} = \begin{pmatrix} k_{s1}+k_{s2}+k_{s3}+k_{s4} & -b_1(k_{s1}+k_{s3})+b_2(k_{s2}+k_{s4}) & -a_2(k_{s3}+k_{s4})+a_1(k_{s1}+k_{s2}) \\ -b_1(k_{s1}+k_{s3})+b_2(k_{s2}+k_{s4}) & b_1^2(k_{s1}+k_{s3})+b_2^2(k_{s2}+k_{s4}) & a_1b_2k_{s2}-a_1b_1k_{s1}+a_2b_1k_{s3}-a_2b_2k_{s4} \\ -a_2(k_{s3}+k_{s4})+a_1(k_{s1}+k_{s2}) & a_1b_2k_{s2}-a_1b_1k_{s1}+a_2b_1k_{s3}-a_2b_2k_{s4} & a_1^2(k_{s1}+k_{s2})+a_2^2(k_{s3}+k_{s4}) \end{pmatrix},
$$

$$
\mathbf{K}_{v12} = \begin{pmatrix} -k_{s1} & -k_{s2} & -k_{s3} & -k_{s4} \\ b_1k_{s1} & -b_2k_{s2} & b_1k_{s3} & -b_2k_{s4} \\ -a_1k_{s1} & -a_1k_{s2} & a_2k_{s3} & a_2k_{s4} \end{pmatrix}, \mathbf{K}_{v21} = \begin{pmatrix} -k_{s1} & b_1k_{s1} & -a_1k_{s1} \\ -k_{s2} & -b_2k_{s2} & -a_1k_{s2} \\ -k_{s3} & b_1k_{s3} & a_2k_{s3} \\ -k_{s4} & -b_2k_{s4} & a_2k_{s4} \end{pmatrix}.
$$

(A.1)

Data Availability

The data used to support the findings of this study are available from the corresponding author upon request.

Conflicts of Interest

The authors declare that they have no conflicts of interest.

Authors' Contributions

Zhenkun Li conceptualized the study, provided software, performed formal analysis, proposed the methodology, and wrote the original draft and edited the manuscript. Weiwei Lin and Youqi Zhang were responsible for funding acquisition, supervised the study, and reviewed and edited the manuscript.

References

[1] C. Zhang, A. A. Mousavi, S. F. Masri, G. Gholipour, K. Yan, and X. Li, "Vibration feature extraction using signal processing techniques for structural health monitoring A review," *Mechanical Systems and Signal Processing*, vol. 177, Article ID 109175, 2022.

[2] O. Avci, O. Abdeljaber, S. Kiranyaz, M. Hussein, M. Gabbouj, and D. J. Inman, "A review of vibration-based damage detection in civil structures: from traditional methods to Machine Learning and Deep Learning applications," *Mechanical Systems and Signal Processing*, vol. 147, Article ID 107077, 2021.

[3] R. Hou and Y. Xia, "Review on the new development of vibration-based damage identification for civil engineering structures: 2010–2019," *Journal of Sound and Vibration*, vol. 491, Article ID 115741, 2021.

[4] X. Jian, Y. Xia, and L. Sun, "Indirect identification of bridge frequencies using a four-wheel vehicle: theory and three-dimensional simulation," *Mechanical Systems and Signal Processing*, vol. 177, Article ID 109155, 2022.

[5] Y. B. Yang, C. W. Lin, and J. D. Yau, "Extracting bridge frequencies from the dynamic response of a passing vehicle," *Journal of Sound and Vibration*, vol. 272, no. 3-5, pp. 471–493, 2004.

[6] Z. L. Wang, J. P. Yang, K. Shi, H. Xu, F. Q. Qiu, and Y. B. Yang, "Recent advances in researches on vehicle scanning method for bridges," *International Journal of Structural Stability and Dynamics*, vol. 22, no. 15, Article ID 2230005, 2022.

[7] P. Singh, S. Mittal, and A. Sadhu, "Recent advancements and future trends in indirect bridge health monitoring," *Practice Periodical on Structural Design and Construction*, vol. 28, no. 1, Article ID 03122008, 2023.

[8] A. Malekjafarian, R. Corbally, and W. Gong, "A review of mobile sensing of bridges using moving vehicles: progress to date, challenges and future trends," *Structures*, vol. 44, pp. 1466–1489, 2022.

[9] J. Sitton, D. Rajan, and B. Story, "Bridge frequency estimation strategies using smartphones," *Journal of Civil Structural Health Monitoring*, vol. 10, no. 3, pp. 513–526, 2020.

[10] Z. Li, W. Lin, and Y. Zhang, "Real-time drive-by bridge damage detection using deep auto-encoder," *Structures*, vol. 47, pp. 1167–1181, 2023.

[11] J. P. Yang and J. Y. Sun, "Pitching effect of a three-mass vehicle model for analyzing vehicle-bridge interaction," *Engineering Structures*, vol. 224, Article ID 111248, 2020.

[12] T. J. Matarazzo, D. Kondor, and P. Santi, "Crowdsourcing bridge vital signs with smartphone vehicle trips," 2020, https://arxiv.org/abs/2010.070266.

[13] A. Di Matteo, D. Fiandaca, and A. Pirrotta, "Smartphone-based bridge monitoring through vehicle–bridge interaction: analysis and experimental assessment," *Journal of Civil Structural Health Monitoring*, vol. 12, no. 6, pp. 1329–1342, 2022.

[14] D. S. Yang and C. M. Wang, "Modal properties identification of damped bridge using improved vehicle scanning method," *Engineering Structures*, vol. 256, Article ID 114060, 2022.

[15] E. J. Obrien, A. Malekjafarian, A. González, E. O'brien, A. Malekjafarian, and A. González, "Application of empirical mode decomposition to drive-by bridge damage detection," *European Journal of Mechanics A Solids*, vol. 61, pp. 151–163, 2017.

[16] S. Sadeghi Eshkevari, T. J. Matarazzo, and S. N. Pakzad, "Bridge modal identification using acceleration measurements within moving vehicles," *Mechanical Systems and Signal Processing*, vol. 141, Article ID 106733, 2020.

[17] J. Li, X. Zhu, and J. Guo, "Bridge modal identification based on successive variational mode decomposition using a moving test vehicle," *Advances in Structural Engineering*, vol. 25, no. 11, pp. 2284–2300, 2022.

[18] N. Jin, V. K. Dertimanis, E. N. Chatzi, E. G. Dimitrakopoulos, and L. S. Katafygiotis, "Subspace identification of bridge dynamics via traversing vehicle measurements," *Journal of Sound and Vibration*, vol. 523, Article ID 116690, 2022.

[19] W. Locke, L. Redmond, and M. Schmid, "Evaluating OMA system identification techniques for drive-by health monitoring on short span bridges," *Journal of Bridge Engineering*, vol. 27, no. 9, Article ID 04022079, 2022.

[20] J. P. Yang and W. C. Lee, "Damping effect of a passing vehicle for indirectly measuring bridge frequencies by EMD technique," *International Journal of Structural Stability and Dynamics*, vol. 18, no. 01, Article ID 1850008, 2018.

[21] J. P. Yang and B. L. Chen, "Rigid-mass vehicle model for identification of bridge frequencies concerning pitching effect," *International Journal of Structural Stability and Dynamics*, vol. 19, no. 02, pp. 1950008–1950015, 2019.

[22] S. Sadeghi Eshkevari, T. J. Matarazzo, and S. N. Pakzad, "Simplified vehicle–bridge interaction for medium to long-span bridges subject to random traffic load," *Journal of Civil Structural Health Monitoring*, vol. 10, no. 4, pp. 693–707, 2020.

[23] N. Shirzad-Ghaleroudkhani and M. Gül, "Inverse filtering for frequency identification of bridges using smartphones in passing vehicles: fundamental developments and laboratory verifications," *Sensors*, vol. 20, no. 4, p. 1190, 2020.

[24] C. Tan, A. Elhattab, and N. Uddin, "Drive-by bridge frequency-based monitoring utilizing wavelet transform," *Journal of Civil Structural Health Monitoring*, vol. 7, no. 5, pp. 615–625, 2017.

[25] C. Tan and N. Uddin, "Hilbert transform based approach to improve extraction of "drive-by" bridge frequency," *Smart Structures and Systems*, vol. 25, no. 3, pp. 265–277, 2020.

[26] Z. Shi and N. Uddin, "Extracting multiple bridge frequencies from test vehicle – a theoretical study," *Journal of Sound and Vibration*, vol. 490, Article ID 115735, 2021.

[27] J. Zhang, C. X. Qu, T. H. Yi, and H. N. Li, "Damage detection for decks of concrete girder bridges using the frequency obtained from an actively excited vehicle," *Smart Structures and Systems*, vol. 27, no. 1, pp. 101–114, 2021.

[28] X. Kong, C. S. Cai, and B. Kong, "Numerically extracting bridge modal properties from dynamic responses of moving vehicles," *Journal of Engineering Mechanics*, vol. 142, no. 6, Article ID 04016025, 2016.

[29] J. Zhan, Z. Wang, X. Kong, H. Xia, C. Wang, and H. Xiang, "A drive-by frequency identification method for simply supported railway bridges using dynamic responses of passing two-axle vehicles," *Journal of Bridge Engineering*, vol. 26, no. 11, Article ID 4021078, 2021.

[30] Y. He and J. P. Yang, "Using acceleration residual spectrum from single two-axle vehicle at contact points to extract bridge

frequencies," *Engineering Structures*, vol. 266, Article ID 114538, 2022.

[31] Y. B. Yang, B. Zhang, Y. Qian, and Y. Wu, "Contact-point response for modal identification of bridges by a moving test vehicle," *International Journal of Structural Stability and Dynamics*, vol. 18, no. 05, Article ID 1850073, 2018.

[32] R. Corbally and A. Malekjafarian, "Examining changes in bridge frequency due to damage using the contact-point response of a passing vehicle," *Journal of Structural Integrity and Maintenance*, vol. 6, no. 3, pp. 148–158, 2021.

[33] H. Wang, T. Nagayama, J. Nakasuka, B. Zhao, and D. Su, "Extraction of bridge fundamental frequency from estimated vehicle excitation through a particle filter approach," *Journal of Sound and Vibration*, vol. 428, pp. 44–58, 2018.

[34] R. Nayek and S. Narasimhan, "Extraction of contact-point response in indirect bridge health monitoring using an input estimation approach," *Journal of Civil Structural Health Monitoring*, vol. 10, no. 5, pp. 815–831, 2020.

[35] Y. He, J. P. Yang, and Z. Yan, "Enhanced identification of bridge modal parameters using contact residuals from three-connected vehicles: theoretical study," *Structures*, vol. 54, pp. 1320–1335, 2023.

[36] Y. B. Yang, H. Xu, Z. L. Wang, and K. Shi, "Using vehicle–bridge contact spectra and residue to scan bridge's modal properties with vehicle frequencies and road roughness eliminated," *Structural Control and Health Monitoring*, vol. 29, no. 8, Article ID e2968, 2022.

[37] Y. Zhan, F. T. K. Au, and J. Zhang, "Bridge identification and damage detection using contact point response difference of moving vehicle," *Structural Control and Health Monitoring*, vol. 28, no. 12, 2021.

[38] R. Corbally and A. Malekjafarian, "A data-driven approach for drive-by damage detection in bridges considering the influence of temperature change," *Engineering Structures*, vol. 253, Article ID 113783, 2022.

[39] International Organization for Standardization, *ISO 8608 Mechanical Vibration Road Surface Profiles-Reporting of Measured Data*, International Organization for Standardization, Geneva, Switzerland, 2nd edition, 2016.

[40] J. T. Li, X. Q. Zhu, S. S. Law, and B. Samali, "A two-step drive-by bridge damage detection using dual kalman filter," *International Journal of Structural Stability and Dynamics*, vol. 20, no. 10, Article ID 2042006, 2020.

[41] H. Wang, T. Nagayama, and D. Su, "Estimation of dynamic tire force by measurement of vehicle body responses with numerical and experimental validation," *Mechanical Systems and Signal Processing*, vol. 123, pp. 369–385, 2019.

[42] Q. Zhang, J. Hou, X. Hu et al., "Vehicle parameter identification and road roughness estimation using vehicle responses measured in field tests," *Measurement*, vol. 199, Article ID 111348, 2022.

[43] R. N. Jazar, *Vehicle Dynamics. 1*, Springer, Heidelberg, Germany, 2008.

[44] H. Xu, Y. H. Liu, Z. L. Wang, K. Shi, B. Zhang, and Y. B. Yang, "General contact response of single-axle two-mass test vehicles for scanning bridge frequencies considering suspension effect," *Engineering Structures*, vol. 270, Article ID 114880, 2022.

[45] J. Zhou, Z. Lu, Z. Zhou et al., "Extraction of bridge mode shapes from the response of a two-axle passing vehicle using a two-peak spectrum idealized filter approach," *Mechanical Systems and Signal Processing*, vol. 190, Article ID 110122, 2023.

[46] J. Hou, Z. Li, Q. Zhang, Ł. Jankowski, and H. Zhang, "Local mass addition and data fusion for structural damage identification using approximate models," *International Journal of Structural Stability and Dynamics*, vol. 20, no. 11, Article ID 2050124, 2020.